

1 **Challenges in modelling spatiotemporally varying phytoplankton blooms in the**
2 **Northwestern Arabian Sea and Gulf of Oman**

4 **S. Sedigh Marvasti¹, A. Gnanadesikan², A.A. Bidokhti³, J.P. Dunne⁴, S. Ghader⁵**

5 [1] Department of Marine Sciences, Science and Research Branch, Islamic Azad University,
6 Tehran, Iran. (safoura.seddigh@gmail.com)

7 [2] Department of Earth and Planetary Sciences, John Hopkins University, Olin Hall, 3400 N.
8 Charles St., Baltimore, MD 21218, USA. (gnanades@jhu.edu)

9 [3] Institute of Geophysics, University of Tehran, Tehran, P. O. Box 14155-6466, Iran.
10 (bidokhti@ut.ac.ir)

11 [4] National Oceanic and Atmospheric Administration/Geophysical Fluid Dynamics
12 Laboratory, 201 Forrestal Rd., Princeton, NJ 08540-6649. (john.dunne@noaa.gov)

13 [5] Institute of Geophysics, University of Tehran, Tehran, P. O. Box 14155-6466, Iran.
14 (sghader@ut.ac.ir)

15 Correspondence to: S. Sedigh Marvasti (safoura.seddigh@gmail.com)

16

17 **Abstract**

18 Recent years have shown an increase in harmful algal blooms in the Northwest Arabian Sea
19 and Gulf of Oman, raising the question of whether climate change will accelerate this trend.
20 This has led us to examine whether the Earth System Models used to simulate phytoplankton
21 productivity accurately capture bloom dynamics in this region- both in terms of the annual
22 cycle and interannual variability. Satellite data (SeaWiFS ocean color) shows two
23 climatological blooms in this region, a wintertime bloom peaking in February and a
24 summertime bloom peaking in September. On a regional scale, interannual variability of the
25 wintertime bloom is dominated by cyclonic eddies which vary in location from one year to
26 another. Two coarse (1°) models with the relatively complex biogeochemistry (TOPAZ)
27 capture the annual cycle but neither eddies nor the interannual variability. An eddy-resolving
28 model (GFDL CM2.6) with a simpler biogeochemistry (miniBLING) displays larger
29 interannual variability, but overestimates the wintertime bloom and captures eddy-bloom

30 coupling in the south but not in the north. The models fail to capture both the magnitude of
31 the wintertime bloom and its modulation by eddies in part because of their failure to capture
32 the observed sharp thermocline/nutricline in this region. When CM2.6 is able to capture such
33 features in the Southern part of the basin, eddies modulate diffusive nutrient supply to the
34 surface (a mechanism not previously emphasized in the literature). For the model to simulate
35 the observed wintertime blooms within cyclones, it will be necessary to represent this
36 relatively unusual nutrient structure as well as the cyclonic eddies. This is a challenge in the
37 Northern Arabian Sea as it requires capturing the details of the outflow from the Persian Gulf-
38 something that is poorly done in global models.

39

40 1 Introduction

41 The region of northwestern Arabian Sea and the Gulf of Oman ($15\text{--}26^{\circ}\text{N}$, $56\text{--}66^{\circ}\text{E}$) is
42 a highly productive region (Madhupratap et al., 1996; Tang et al., 2002), with satellite
43 estimates of carbon export of $137\text{ gC/m}^2/\text{yr}$, much higher than the $\sim 80\text{ gC/m}^2/\text{yr}$ found in the
44 Subpolar North Atlantic and Pacific (Dunne et al., 2007). Peak chlorophyll-a concentrations
45 exceed 0.7 mg/m^3 in this region (Fig. 1a).

46 This region may be changing in important ways. In both the Persian Gulf and the Gulf
47 of Oman, there is evidence that harmful algal bloom (HABs) and their impacts are increasing
48 (Richlen et al., 2010). HAB occurrences have been more frequently reported in the Gulf of
49 Oman rather than Persian Gulf. A total of 66 red tide events (mostly dominated by *Noctiluca*
50 *scintillans*) have been recorded between 1976 and 2004 including 25 blooms resulting in mass
51 mortality of fish and marine organisms. Reasons for the increase in blooms include
52 aquaculture activities and industrial and sewage inputs, natural dispersal and human-aided
53 transport, long-term increases in nutrient loading and global expansion of species (Richlen et
54 al., 2010) as well as global climate change (Goes et al., 2005). The latter paper suggested that
55 increasing blooms were driven by an increase in the strength of the Asian monsoon.

56 Evaluating such a possibility and extending it into the future requires the use of Earth
57 System Models. However, such projections will only be as good as the models on which they
58 are based. In this paper we examine several models run at the Geophysical Fluid Dynamics
59 Laboratory in the Arabian Sea. We consider numerical results from four different 3D global
60 Earth system models, which we denote CORE-TOPAZ, Coupled-TOPAZ, Coupled-BLING
61 and the Geophysical Fluid Dynamics Laboratory Climate Model version 2.6 (CM2.6)

62 (miniBLING). The first two of these models use the relatively complex TOPAZ
63 biogeochemistry, but have low resolution and do not resolve eddies, the third has a simplified
64 biogeochemistry which does not carry phytoplankton biomass as a separate variable while the
65 last model has very high resolution, but also a simpler biogeochemistry. Biological cycling in
66 CM2.6 is simulated using a modified version of the Biogeochemistry with Light Iron
67 Nutrients and Gasses (BLING) model (Galbraith et al., 2010) called mini-BLING.

68 The seasonal cycle is an important metric for models to be able to simulate. The
69 Arabian Sea is influenced by a reversing monsoonal cycle (Wang and Zhao, 2008), an
70 evaporative fresh-water flux over most of the basin, and an annual mean heat gain (Banse and
71 McClain, 1986; Fischer et al., 2002). In summer (June-September), the southwest Monsoon
72 (SWM) blows strongly across the northwestern Arabian Sea (Al-Azri et al., 2010). Driven by
73 a land-sea pressure gradient, the SWM is a large-scale feature of the atmospheric circulation
74 of the tropics, extending from a surface pressure high near 30° S in the southern hemisphere
75 northward to the surface low over Asia (Anderson and Prell, 1993). During the SWM, winds
76 are steered by the East African highlands to form a strong low level atmospheric jet, referred
77 to as the Findlater Jet (Bartolacci and Luther, 1999; Honjo et al., 2000), which crosses the
78 Equator over the Indian Ocean and blows over the Arabian Sea parallel to the Omani
79 coastline in a northeast direction (Honjo et al., 2000). The orientation of the Findlater Jet
80 parallel to Omani coast leads to coastal upwelling along the coast and downwelling on the
81 eastern side of the Jet in the middle of Arabian Sea. This upwelling provides nutrients to the
82 surface layer (Fig. 1b) (Al-Azri et al., 2013; Kawamiya and Oschlies, 2003; Madhupratap et
83 al., 1996; Murtugudde et al., 2007; Veldhuis et al., 1997; Wang and Zhao, 2008). The SWM
84 does not destabilize the surface layers, which are fairly stable in northern summer (Fig. 1c).

85 The Northeast Monsoon (NEM), which happens from December through February, is
86 not as strong as the SWM (Dickey et al., 1998; Shalapyonok et al., 2001; Veldhuis et al.,
87 1997). Ocean surface wind stress is lower (0.032 N/m² in NEM compared to 0.127 N/m² in
88 SWM), and does not lead to upwelling like the SWM along the Omani coast. However,
89 negative heat flux results in a destabilizing buoyancy flux, subsequent convective overturning
90 (Barimalala et al., 2013; Kawamiya and Oschlies, 2003), and deepening and cooling to a
91 depth of ~60m (Fig. 1c, 1d). This brings up nutrients and fuels a wintertime bloom. In
92 addition, as shown in Fig. 1d in wintertime bloom the mixed layer depth (MLD) is deeper
93 than summer.

94 A second metric of the bloom dynamics is the relationship between the blooms and
95 mesoscale eddies (Al-Azri et al., 2013; Dickey et al., 1998; Hamzehei and Bidokhti, 2013;
96 Shalapyonok et al., 2001; Gomes et al., 2005). The confluence of the Persian Gulf outflow
97 current and the East Arabian Sea Current parallel to Omani and Yemeni coastlines in Arabian
98 Sea leads to formation of a frontal zone and formation of persistent eddies in the region.
99 Because the size of eddies is comparable to the width of the Gulf of Oman, they can affect
100 mixing and transport of biota on a basin scale (Fischer et al., 2002; Piontkovski et al., 2012).
101 Piontkovski et al. (2012) suggested that the increased amplitude of the seasonal cycle of
102 chlorophyll-a might be associated with the increased variability of mesoscale eddy kinetic
103 energy (EKE) per unit mass in the Gulf of Oman or in the western Arabian Sea. Gomes et al.
104 (2008) noted potential anticorrelation between sea surface height and chlorophyll, but did not
105 find a consistent relationship over time.

106 Gaube et al. (2014) provide a global overview of how eddies influence chlorophyll
107 blooms. They find that the effect of mesoscale eddies on the chlorophyll bloom varies both
108 temporally and spatially. They identify four particular mechanisms that can be distinguished
109 by linking sea surface anomalies to chlorophyll, namely eddy stirring, trapping, eddy
110 intensification, and Ekman pumping. Although Gaube et al. (2014) find a negative correlation
111 between chlorophyll and SSH in the Arabian Sea, they do not analyse which of these
112 mechanisms is involved in this region, nor do they quantify the extent to which this
113 correlation varies over the course of the season.

114 Resplandy et al. (2011) indicated that the spatial variability associated with mesoscale
115 eddies in the Arabian Sea produces spatial variability in the bloom and that another source of
116 variability is found to be restratification at these structures. Advection from coastal region is
117 identified as the mechanism providing nutrients in summer, while vertical velocities
118 associated with mesoscale structure are found to increase the overall nutrient supply.
119 However, this work does not make clear how the spatial distribution of the eddy supply is
120 related to the eddies.

121 The structure of this paper is as follows: all datasets including ocean color data and
122 altimeter data are explained in section 2 of the paper along with the specification four
123 different 3D global Earth system models. In section 3, the remote sensing results are used to
124 study the spatiotemporal variability of chlorophyll-a in mesoscale structures in the study
125 region. We find a seasonal relationship between SSHA and chlorophyll such that cyclonic

126 eddies are associated with blooms, but only during the winter. This means that interannual
 127 variability in blooms will be shaped by mesoscale eddy activity and may not be predictable.
 128 Results of the 3D global Earth system models are discussed in section 4. Annual cycles of
 129 variation of chlorophyll-a and nutrients for all GFDL models within the whole region are
 130 compared against the corresponding satellite results and field measurements. The models tend
 131 to overestimate wintertime productivity, in large part due to excessive mixing. They also fail
 132 to explain the bloom-SSHA relationship except in a few special cases. We argue that the
 133 eddies act to modulate turbulent mixing of nutrients to the surface- a mechanism not
 134 emphasized in previous literature. However, this can only occur if there is a strong and
 135 relatively shallow nutricline. Since the model only simulates such a feature in the Southern
 136 Arabian Sea, it does not capture the observed relationship between SSH and biology. Both the
 137 overestimation of the wintertime bloom and the failure to predict its modulation by eddies can
 138 thus be traced to difficulties in modeling the stratification of the Northwest Arabian Sea, most
 139 likely as a result of a failure to properly simulate overflows.

140

141 **2 Description of data and models**

142 **2.1 Satellite products**

143 We examine the relationship of blooms and eddies using the GSM5 Maritorena et al. (2002)
 144 product based on the SeaWiFS (Sea-viewing Wide Field-of-view Sensor) ocean color data
 145 and Sea Surface Height Anomaly (SSHA), based on altimeter data acquired from the
 146 Archiving, Validation and Interpretation of Satellite Oceanographic (AVISO) Data Center
 147 (<http://www.aviso.oceanobs.com>). The SSH anomaly is calculated relative to the annual
 148 cycle.

149 The GSM algorithm represents the normalized water leaving radiance $L_{wN}(\lambda)$ at multiple
 150 wavelengths as a nonlinear function, as following (Maritorena et al., 2002),

$$151 \hat{L}_{wN}(\lambda) = \frac{tF_0(\lambda)}{n_w^2} \sum_{i=1}^2 g_i \left\{ \frac{b_{bw}(\lambda) + b_{bp}(\lambda_0)(\lambda/\lambda_0)^{-\eta}}{b_{bw}(\lambda) + b_{bp}(\lambda_0)(\lambda/\lambda_0)^{-\eta} + a_w(\lambda) + Chl a_{ph}^*(\lambda) + a_{cdm}(\lambda_0) \exp[-S(\lambda - \lambda_0)]} \right\}^i \quad (1)$$

152 where t is the sea-air transmission factor, $F_0(\lambda)$ is the extraterrestrial solar irradiance, n_w is the
 153 index of refraction of the water, seawater backscatter $b_{bw}(\lambda)$, absorption $a_w(\lambda)$, a_{ph}^* is the
 154 chlorophyll-a (*chl*) specific absorption coefficient, S is the spectral decay constant for

155 absorption by chromophoric dissolved organic materials (CDOM), η is the power-law
156 exponent for the particulate backscattering coefficient, and λ_0 is a scaling wavelength (443
157 nm). The cdm absorption coefficient [$a_{cdm}(\lambda_0)$], and slope factor S then determine the
158 absorption across a range of wavelengths while the particulate backscatter coefficient [$b_{bp}(\lambda_0)$]
159 and coefficient η constrain the scattering. Letting λ_0 be 443 nm assuming that all terms other
160 than *chl*, [$a_{cdm}(\lambda_0)$] and $b_{bp}(443\text{nm})$ are constant, one can then use the water leaving radiance
161 to invert for *chl*, a_{cdm} , and backscatter. One limitation of this approach is that if the inherent
162 optical properties vary with time, this variation will introduce errors into the estimate.
163 Following Behrenfeld et al. (2005), we convert the backscatter coefficient into units of
164 particulate carbon biomass using the relationship $p_{carb}=13000(b_{bp}-0.00035)$.

165 Satellite-based remote sensing is the only observational method suitable for measuring
166 physical and biological properties over large regions of the ocean. However, satellite ocean
167 color and SST are limited to surface distributions and provide no information about the
168 vertical structure within the ocean (McGillicuddy et al., 2001). Additionally acquiring data
169 requires cloud-free viewing of the ocean surface, which as we will see is a problem in this
170 region at certain times of the year. This lack of information motivates our examination of
171 numerical models, which ideally could be used to provide estimates of the ocean state when
172 observations are sparse as well as to extrapolate both vertically and into the future.

173

174 **2.2 Numerical models**

175 Numerical results are presented in this paper based on the output of four different 3D
176 global Earth system models, which we denote CORE-TOPAZ, Coupled-TOPAZ, Coupled-
177 BLING/miniBLING and GFDL CM2.6 (miniBLING). The first two of these models use the
178 relatively complex TOPAZ biogeochemistry, but have low resolution and do not resolve
179 eddies. The third uses two simplified biogeochemistry codes (BLING and miniBLING) which
180 do not carry phytoplankton biomass as a separate variable while the last model has very high
181 resolution and uses the miniBLING simplified biogeochemistry. Below, we describe the
182 different physical models, followed by a summary of the biogeochemical codes run within
183 these models.

184

185 2.2.1 Physical model description

186

187 The ocean-ice model used in the CORE-TOPAZ model follows the corresponding
188 components of the GFDL CM2.1 global coupled climate model (Delworth et al., 2006). The
189 vertical resolution ranges from 10 m over the top 200 m to a maximum thickness of 250 m at
190 5500 m depth with 50 layers in all. The meridional resolution is 1° , whereas the zonal
191 resolution varies between 1° in mid-latitudes and $1/3^{\circ}$ at the equator. North of 65° , a tripolar
192 grid is employed to avoid singularity arising from convergence of meridians at the North
193 Pole. Up-to-date parameterizations of mixed-layer dynamics, isopycnal mixing, advection by
194 subgrid-scale eddies, bottom topography, bottom flows, and lateral viscosity are included- for
195 more detail see Griffies et al. (2005) and Gnanadesikan et al. (2006). Both the dynamics and
196 thermodynamics sea ice are simulated with five thickness classes of sea ice being resolved.

197 In the CORE-TOPAZ model, surface forcing is set using the Coordinated Ocean-ice
198 Reference Experiment (CORE) protocol (Griffies et al., 2009), where the inputs for
199 calculating surface fluxes are taken from an atmospheric analysis dataset adjusted to agree
200 better with in situ measurements. Sensible and latent heat fluxes are then calculated using
201 bulk formulae. Freshwater forcing is given by a combination of applied precipitation,
202 evaporation computed using bulk fluxes, and a correction diagnosed to restore surface
203 salinities in the top 10 m to climatological monthly values over 60 d. Hence, the fluxes
204 forcing the CORE runs could be thought of as “best guess” observationally based estimates.
205 Such a prescription omits important feedbacks whereby the atmosphere ensures that rainfall
206 and evaporation are consistent with each other, although the restoring correction is a crude
207 representation of these feedbacks. We use the version of the model described in Gnanadesikan
208 et al. (2011), which analyzed different modes of interannual variability in biological cycling
209 across the Pacific Ocean.

210 The Coupled-TOPAZ model corresponds to the control simulation of the GFDL
211 ESM2M submitted as part of the IPCC AR5 process (Dunne et al., 2012). In this model the
212 ocean is coupled to the atmosphere, land, and sea ice components. Gnanadesikan et al. (2014)
213 discuss the behavior of this model in the North Atlantic, but its behavior in the Arabian Sea
214 has not been previously analyzed. Two additional version of this model, referred to here as
215 Coupled-BLING, was run using the BLING and mini-BLING biogeochemical models

216 described below, but with the light field given by the TOPAZ code. The difference between
217 the 1-degree models emphasizes differences due to biological formulation.

218 The ocean component of ESM2M employs the MOM4p1 code of Griffies et al. (2009)
219 which largely mimics the CM2.1 ocean (identical horizontal and vertical resolution and
220 parameterization of mixing). However, ESM2M ocean uses a rescaled geopotential vertical
221 coordinate (z^* ; Adcroft et al., 2004; Stacey et al., 1995) for a more robust treatment of free
222 surface undulations. The ESM2M implementation includes updates to the K-profile
223 parameterization (Large et al., 1994) based on Danabasoglu et al. (2006), as well as model-
224 predicted chlorophyll modulation of short-wave radiation penetration through the water
225 column. ESM2M also includes completely novel parameterizations relative to CM2.1, such as
226 parameterization of submesoscale eddy-induced mixed layer restratification (Fox-Kemper et
227 al., 2008). Instead of prescribed vertical diffusivity for interior mixing (Bryan and Lewis,
228 1979), ESM2M employs the Simmons et al. (2004) scheme along with a background
229 diffusivity of $1.0 \times 10^{-5} \text{ m}^2 \text{ s}^{-1}$ in the tropics and $1.5 \times 10^{-5} \text{ m}^2 \text{ s}^{-1}$ poleward of 30° latitude
230 following a *tanh* curve.

231 The Geophysical Fluid Dynamics Laboratory Climate Model version 2.6 (CM2.6) is a
232 high-resolution eddy-resolving model. This model has the same atmosphere model and ocean
233 Physics as CM2.5 (Delworth et al., 2012). CM2.6's ocean component has higher horizontal
234 resolution than CM2.5, with grid spacing, which is changeable from 11 km at the equator to
235 less than 4 km at very high latitudes. This means that the model is capable of resolving eddy
236 features in the tropics, as we will see below.

237

238 2.2.2 Biogeochemical Cycling codes

239 The TOPAZ code (Tracers of Ocean Productivity with Allometric Zooplankton code
240 of Dunne et al., 2010), keeps track of five inorganic nutrients used by phytoplankton: nitrate
241 and ammonia, inorganic phosphate, silicate, and dissolved iron. Additionally, the model
242 carries three other dissolved inorganic tracers: dissolved inorganic carbon, alkalinity and
243 dissolved oxygen. Based on the work of Dunne et al. (2007), the model also keeps track of
244 fine lithogenic material, which plays a role in ballasting organic material and delivering it to
245 the sediment (Armstrong et al., 2002; Klaas and Archer, 2002). The five inorganic nutrients
246 are taken up in different ways by three classes of phytoplankton: small, large and

247 diazotrophic. A comprehensive description of TOPAZ v2 can be found in the supplemental
248 material of Dunne et al. (2013).

249 TOPAZ is unusual among comprehensive Earth System Models in that it uses a highly
250 parameterized version of grazing. Instead of grazers being explicitly simulated, grazing rates
251 are simply taken as a function of phytoplankton biomass, with different power-law
252 dependence for small and large phytoplankton. The grazing formulation was fit to about 40
253 field sites to produce a size structure that transitions realistically between being dominated by
254 small phytoplankton and low particle export ratio at low levels of growth and large
255 phytoplankton and high particle export ratio in nutrient and light-replete conditions. At
256 equilibrium, the resulting parameterization produces biomass that is a function of growth rate
257 (linear for small plankton, cubic for large). A similar scaling in particle size spectrum was
258 seen across ecosystems by Kostadinov et al. (2009). In contrast to models that explicitly
259 simulate zooplankton, it does not depend poorly known zooplankton behavioral parameters
260 (such as handling efficiency or grazing half-saturation) on to the details of how different
261 trophic levels interact.

262 Even though it does not simulate zooplankton explicitly, TOPAZ still carries over two
263 dozen tracers, making it extremely expensive to run in high-resolution simulations. For this
264 reason Galbraith et al. (2010) developed the Biogeochemistry with Light Iron Nutrients and
265 Gasses (BLING) model (Galbraith et al., 2010), which parameterizes the entire ecosystem.
266 The original version of BLING has only five explicit tracers: dissolved inorganic phosphorus
267 (PO_4), dissolved organic phosphorus (DOP), dissolved Iron (Fe), DIC (dissolved inorganic
268 carbon), and oxygen (O_2). It includes the impacts of macronutrient and micronutrient
269 limitation and light limitation on phytoplankton by using these to calculate a growth rate.
270 Using the same machinery as TOPAZ, it then uses this growth rate and implicit treatment of
271 community structure to estimate phytoplankton biomass, and uses this biomass to calculate
272 the rate at which nutrient is taken up by plankton and cycled through the ecosystem.

273 The miniBLING code (Galbraith et al., 2015) represents a further simplification. In
274 this model the iron field is taken from a lower-resolution version of the model (an
275 approximation which has limited impact in the Arabian Sea, where phytoplankton are
276 generally not iron-limited) and so Fe is not treated prognostically. Additionally the DOP pool
277 is eliminated. Simulations using the ESM2M physical model show that control simulations of
278 oxygen and surface nutrients produced by miniBLING and BLING models are very similar to

279 those produced in the same model with TOPAZ (Galbraith et al., 2015). This manuscript also
280 shows that BLING and miniBLING simulate very similar patterns of oxygen change and
281 anthropogenic uptake in a simulation where CO₂ is increased by 1% per year until it doubles.

282 It should be noted that simplified BLING and miniBLING codes neglect some
283 processes that may be important. Only nonliving components are advected and mixed by the
284 ocean circulation, which could result in inaccurate distribution of biology in frontal regions at
285 high resolution. Also, the rich behavior of the nitrogen cycle with its interaction with iron,
286 phosphorus and oxygen cannot be simulated with one macronutrient tracer Behrenfeld (2010).
287 Specifying iron limitation, as done in miniBLING, may also have some impacts in our region.
288 As extensively discussed by Naqvi et al., (2010) there is a possibility of iron limitation over
289 the southern parts of the Omani shelf and in the offshore region during the latter part of the
290 Southwest Mansoon, which can result in high nitrate-low chlorophyll conditions. The western
291 equatorial and southern tropical region of the Indian Ocean are iron-limited and the Arabian
292 Sea (southern parts) may become iron-limited under strong upwelling conditions (Wiggert et
293 al., 2006).

294

295 **3 Remote sensing results**

296 **3.1 Interannual variability**

297 We begin by using the GSM5 satellite data to examine the annual cycle and interannual
298 variability in two different regions, the whole NW Arabian Sea (56°-66° E, 15°-26° N) and a
299 smaller region including the Gulf of Oman, (60°-62° E, 22°-26° N). As shown in Fig. 2 (a) to
300 (c) for whole region, clear annual cycles of chlorophyll-a, backscattering and CDOM are
301 observed. Even larger annual cycles of variation of chlorophyll-a, backscattering and CDOM
302 are seen in the smaller region, as shown in Fig. 2 (d) to (f). More pronounced interannual
303 variability is observed in the smaller region as opposed to the larger region.

304 The annual variations of all parameters are broadly consistent with each other. The maximum
305 values associated with the summer bloom are generally seen in September, with values of 1.0
306 mg/m³, 50 mgC/m³, and 0.1 m⁻¹ for chlorophyll, particulate carbon and CDOM, respectively,
307 within the whole region. Within the smaller region the values are 1.25 mg/m³, 65 mgC/m³, and
308 0.125 m⁻¹ for chlorophyll, particulate carbon, and CDOM, respectively. For two years of 2001
309 and 2002, the particulate carbon values (~90 mgC/m³) are much higher than the average of the

310 other months over both regions, but the chlorophyll does not show pronounced peaks. A
311 winter bloom is also pronounced in February as a second maximum in a yearly cycle, where
312 the magnitudes are about 0.07 mg/m^3 , 40 mgC/m^3 , and 0.07 mgC/m^3 for chlorophyll,
313 particulate carbon and CDOM, respectively, within the whole region, and about $0.09\sim1.5$
314 mg/m^3 , $55\sim80 \text{ mgC/m}^3$, and $0.11\sim0.14 \text{ mgC/m}^3$ for chlorophyll, particulate carbon and
315 CDOM, respectively, within the smaller region. That the summer bloom in the both regions is
316 stronger than the winter bloom has been discussed by Al-Azri et al. (2010), and Levy et al.
317 (2007).

318 **3.2 Variability of Chlorophyll-a in Mesoscale Structures**

319 Mesoscale structures can be seen in the Northwest Arabian Sea in both the SeaWiFS
320 chlorophyll-a distribution and AVISO sea surface height anomaly. Over the course of 2001
321 (Fig. 3), both a summer bloom (which most likely starts in August and ends in ~October) and
322 a winter bloom (which starts in January and goes away in April) can be seen in chlorophyll-a.
323 In March, the last month of the winter bloom, chlorophyll-a concentrations are high over the
324 entire region in both the anticyclones (warm eddies with positive SSHA) and the cyclones
325 (cold eddies with negative SSHA). The observed bloom in March terminates abruptly in
326 April, although the observations show that eddies are still active in the region. In June, July
327 and August, the satellite ocean color data is not available due to excessive cloudiness. In
328 September, the last month of the summer bloom, most of the region including cyclones and
329 anticyclones and coastal regions had high chlorophyll-a concentration. However in the
330 following months the bloom persists only within the cold eddies and disappears over the
331 warm eddies (a phenomenon also seen in Sargasso Sea by McGillicuddy et al., 2001). The
332 relationship between sea surface chlorophyll-a and eddies for the other years between 1998
333 and 2005 during the month of November, is shown in Fig. 4. The relationship between
334 blooms and SSHA is clear and striking. Note particularly the difference between 1998 and
335 2001, when the location of high and low chlorophyll regions switches relative to the Ras al
336 Hadd. This difference in bloom location is perfectly reflected in the different patterns of the
337 eddies.

338 **3.3 Chlorophyll-Sea Surface Height Anomaly (SSHA) cross-correlation**

339 The seasonal relationship between chlorophyll and SSHA can be seen in monthly variation of
340 the spatial cross-correlation between the two variables over the entire northwest Arabian Sea.

341 chlorophyll-SSHA cross-correlations between 1998 and 2005 in the satellite data are shown in
342 Fig. 5a. To check that the chlorophyll results are not an artifact of the remote sensing
343 inversion, two other related parameters, the backscattering coefficient (BBP) and
344 chromophoric dissolved organic matter (CDOM) are also cross-correlated with SSHA, as
345 depicted in Figs. 5b and c. The results show consistent annual cycles of variation in the cross-
346 correlation of all three variables. This suggests a repeatable yearly phenomenon in the region
347 as discussed in the previous sections. The cross-correlation results over the 8 years of study
348 shows that there are several months (i.e. November-December) with relatively high anti-
349 correlation for most of the years and also several other months (i.e. April-May) with no or
350 even low positive correlation.

351 The averaged climatological monthly cross-correlation with SSHA and climatological
352 monthly values between 1998 and 2005 are shown in Fig. 6 for all parameters. Two blooms
353 ending in March (winter) and September (summer) are seen. At the peak of the blooms the
354 average cross-correlation values are very low due to the existence of blooms in both cyclones
355 and anticyclones. The months after the winter and summer blooms show a clear difference in
356 the correlation. After the winter bloom (typically April and May), the cross-correlation is
357 positive or very small, which suggests no relation between the mesoscale eddies, and the
358 blooms. As discussed in Kumar et al. (2001), low primary production is observed after
359 termination of winter cooling during Spring Inter-Monsoon (SIM) (Gomes et al., 2008). This
360 result would be also consistent with SIM producing weak atmospheric forcing in the region.

361 In contrast, after the summer bloom (typically October-December) as the average values of
362 chlorophyll-a decrease, chlorophyll and SSHA become relatively highly anti-correlated. The
363 reason for the anti-correlation is the persistence of chlorophyll at the regions with negative
364 SSHA that typically considered to be cyclonic (cold) eddies and disappearance of
365 chlorophyll-a in positive SSHA that assumed to be anti-cyclonic (warm) eddies. Particle
366 backscatter also provides almost same cross-correlation and average value results suggesting
367 that the chlorophyll-a signal does not result purely from photo-adaptation. Moreover, the
368 CDOM-SSHA cross-correlation shows the same patterns for bloom times but typically shows
369 lower correlation.

370 The spatial relationship between blooms and eddies seen in the Northern Arabian Sea can be
371 compared with the patterns noted by Gaube et al. (2014). Their eddy stirring mechanism
372 involves advection of high and low chlorophyll signals around an eddy, resulting in a low

373 which is offset from the center of an anticyclone and a high which is offset from the center of
374 a cyclone. Ekman pumping would be expected to produce negative anomalies in cyclones
375 with a positive “halo” and positive anomalies in anticyclones with a negative “halo” (Gaube
376 et al. (2014), Fig. 2). Trapping of chlorophyll involves eddies retaining the properties that
377 they had when shed from a boundary current, which would generally imply low values in
378 anticyclones and high values in cyclones. Eddy intensification would be expected to produce
379 the same picture, as cyclones would see rising nutriclines in the center but anticyclones would
380 see deepening nutriclines. The basic picture seen in the Arabian Sea is inconsistent with the
381 first two mechanisms but is potentially consistent with the second two. However, without in-
382 situ data it is impossible to validate either of these mechanisms.

383

384 **4 Numerical modelling results**

385 **4.1 Temporal variability**

386 Annual cycles of variation of chlorophyll-a , phosphate and nitrate for all GFDL models are
387 shown in Fig. 7a to c within the whole region and compared against the corresponding GSM5
388 satellite results or WOA09. Note that the eight years of the model output, selected as the last
389 eight years of the run, would not be expected to correspond to the eight actual years in the
390 satellite data. The annual cycles of chlorophyll-a and biomass are quite similar to each other
391 in all GFDL models, insofar as they show two distinct blooms in yearly cycle. The maximum
392 values that can be considered as a winter bloom in the whole region are mostly seen around
393 February (Piontkovski et al., 2011), with values of 0.32–0.38, 0.48–0.62, 1.0–2.0, 1.5–2.2,
394 0.8–1.6, 0.6–0.75 mgm^{-3} for chlorophyll in CORE-TOPAZ, Coupled-TOPAZ, CM2.6
395 (miniBLING), miniBLING (Low resolution), BLING and satellite data, respectively. A
396 summer bloom is also pronounced in September as a second maximum in the yearly cycle
397 over the whole region, with peak magnitudes of about 0.52, 0.66, 0.7–0.9, 0.75–1.0, 2–1.2,
398 0.6–0.75, 0.75–1.3 mgm^{-3} for chlorophyll across the different datasets.

399 Notice the results from the BLING model run in the coarser resolution ESM2M code (purple
400 lines). The differences between BLING and miniBLING (light blue lines) in this code are just
401 due to having fixed iron in miniBLING. The light field in these ESM2M runs is computed
402 from using TOPAZ-derived chlorophyll, so that all three models see identical physical
403 conditions. Both BLING and miniBLING in ESM2M produce an asymmetry in chlorophyll

404 between February and September that is similar to that produced in CM2.6 miniBLING. This
405 asymmetry is not seen in TOPAZ. Analysis of what drives this asymmetry shows that it is not
406 straightforward. All of the model runs show an asymmetry in the nutrient concentrations that
407 is in the opposite direction as the observations, with higher nutrients in February than in
408 September, as shown in Fig 7b. As we will show later in the manuscript, this is probably
409 associated with the models mixing to excessive depth during the wintertime. However, in
410 TOPAZ this does not produce an asymmetry in chlorophyll, while in BLING and miniBLING
411 it does. There are two possible reasons for this:

412 1) The equilibrium assumption, which means that biomass in both BLING and miniBLING is
413 not directly simulated. In TOPAZ, the growth of plankton during the spring is limited by the
414 biomass of phytoplankton, whereas in the fall TOPAZ continues to have higher heterotrophic
415 biomass (diagnosed from growth rates over previous months) that then grazes the plankton. In
416 BLING and miniBLING, by contrast, the biomass responds almost instantaneously to changes
417 in growth conditions.

418 2) Different handling of light limitation. In TOPAZ light limitation is calculated using the
419 instantaneous local light, whereas in BLING it is calculated using the mixed layer average
420 light. Preliminary results with a very coarse resolution model using BLING show that this
421 reduces the summer-winter asymmetry slightly, but is not sufficient to make the February
422 bloom smaller than the September bloom.

423 It is likely that all three of these factors- too deep winter mixed layers leading to too high
424 nutrients, too little light limitation and instantaneous response to changes in growth
425 conditions, are all responsible for the overly strong blooms in boreal winter in the Arabian
426 Sea.

427 To get a better sense of the mechanisms driving the blooms in the model, the biomass (mol P
428 kg⁻¹) is compared with the light intensity in the mixed layer and the light-saturated
429 photosynthesis rate (carbon specific) (s⁻¹) in Figs. 8a and b for January of year 195. The two
430 terms in Fig. 8 are the two terms in the model that affect growth rate. Because biomass in the
431 miniBLING model is a function of growth rate only, it is in fact sufficient to understand what
432 drives the growth in the model. The biomass production and mixed layer light intensity (Fig.
433 8a) are not meaningfully correlated parameters. On the other hand, the biomass and the light-
434 saturated carbon specific growth rate (Fig. 8b; indicating the degree of nutrient limitation) are
435 positively correlated. From this, it can be concluded that the blooms in this region are more

436 driven by nutrient rather than light, consistent with, for example, Gomes et al. (2008). This
437 suggests in turn that it is likely biases in nutrient supply that drive biases in productivity.

438 We can get more insight into nutrient biases by examining the individual tendency terms
439 associated with advection, vertical diffusion and subgridscale eddy fluxes and time rate of
440 change of nutrients. For simplicity, in this paper we combine the vertical diffusive flux
441 associated with small-scale mixing with that due to the mixed layer parameterization. Fig. 10
442 shows PO₄ advection, diffusion and tendency flux terms for the whole region (56°-66°E, 15°-
443 26°N) over a typical year, which is averaged flux values over the upper 50 meter calculated
444 for phosphate (PO₄). The results show that the dominant source in whole region during the
445 winter bloom is diffusion, suggesting the model predicts excessively strong mixing during the
446 wintertime. By contrast, the advection dominates diffusion in summer bloom in supplying the
447 nutrients particularly during the months of July and August and the fact that the summertime
448 bloom is close to observations suggests that the model correctly simulates this wind-driven
449 upwelling.

450 In addition to having annual cycles that are different from observations, the models also differ
451 from data in terms of interannual variability. As shown in Fig. 10, low-resolution models
452 (CORE- and coupled-TOPAZ) provide an almost uniform seasonal coefficient of variation
453 (mean C.o.Vs are 0.15 and 0.18, respectively), while both data and eddy resolving CM2.6
454 models show higher interannual variability and seasonal changes (mean C.o.Vs are 0.35 and
455 0.5, respectively). The C.o.Vs are particularly higher during the winter and summer blooms in
456 the observations, while the low-resolution models do not see these signals. In other words, the
457 low-resolution models fail to get enough variability, while the high-resolution models produce
458 too much interannual variability. Together with the Fig. 4, this statistical analysis suggests
459 that eddies are necessary to explain the variability in the data as opposed to the low-resolution
460 models. Below, we examine the relationship of eddies and blooms in the high-resolution
461 models.

462

463 **4.2 Blooms and sea surface height in CM2.6**

464 **4.2.1 Large-scale correlation**

465 The relationship between SSHA and chlorophyll is quite different in the model as compared
466 to the satellite. Monthly variation in the cross-correlation of chlorophyll and SSHA for eight
467 consequent years in CM2.6 is shown in Fig. 11. As in the remote sensing, the model shows
468 annual cycles of variation in the cross-correlation, suggesting a repeatable yearly phenomenon
469 in the region. However the structure of this annual cycle is not consistent with the satellite
470 data. The model predicts several months (i.e. March-August) with anti-correlation for most of
471 the years, but with values less than 0.5, smaller than the peak anti-correlation values in
472 satellite results. The model also predicts that several other months (i.e. October-February)
473 should have no or even positive correlation, while the satellite shows strong negative
474 correlations during these months.

475

476

477 **4.2.2 Blooms in Mesoscale Structures**

478 Why does the GFDL CM2.6 model not produce the same relationship between SSHA and
479 chlorophyll as the satellite? We can gain some insight by examining snapshots of the two
480 fields. In Figs. 12a and b, sea surface chlorophyll-a concentration and sea surface height
481 anomaly (SSHA) are shown at two snapshots of time, November 9th and December 28th for
482 model year 195. Comparing the figures with the corresponding satellite results in Fig. 3 for
483 the months of November and December, we see that the southern part of the GFDL model is
484 more similar to the satellite data, with high concentrations of chlorophyll-a tending to be
485 located at the center of cyclones. In contrast, in the northern part of the region, the GFDL
486 model predicts high chlorophyll at the edges of the cyclones as well as in the center of
487 anticyclones. The eddy structures have smaller diameters in GFDL results than the field
488 observations, though it is not clear whether this represents smoothing in the AVISO product
489 or some physical weakness of the model.

490 We now focus on the few examples in our model output where chlorophyll blooms are found
491 in the center of cyclonic eddies. These are denoted as E1 and E2 in Figs. 12a and b. To track
492 the movement of the selected eddies, E1 and E2, over the time from November 9th to

493 December 28th, modeled chlorophyll and SSHA are shown in Figs. 12c and d along two
494 different latitudes, 16°N (for E1) and 19°N (for E2). Fig. 12c shows that E1 moved westward
495 during this period of time, and that the chlorophyll concentration was kept high within the
496 central part of the eddy. E1 appears to be created by the passage of a cyclone, similar to the
497 eddy observed by Wang and Zhao (2008) in the aftermath of Cyclone Gonu. Similarly, as
498 shown in Figs. 12d, E2 was a persistent eddy with both central and edge blooms during the
499 month of November that started to move towards the west during the December along 19°N.
500 However, at other latitudes, the largest blooms offshore are found along gradients in SSH
501 rather than being associated with maxima or minima. This suggests a different mechanism for
502 producing blooms in the model. Following Gaube et al. (2014), it appears that the eddy
503 stirring mechanism is dominant. Satellite data (i.e. see Fig. 3 for the month of May) provide
504 some hints for the existence of advective chlorophyll plumes being advected away from
505 coastal regions. As shown in Figs. 12a and b, high velocities in the marginal region between
506 adjacent cyclonic and anticyclonic eddies can cause such plumes in the GFDL models as well.

507 Why is the model only able to simulate the relationship between SSH and chlorophyll in the
508 Southern part of the domain? We hypothesize this is due to differences in stratification
509 between the two regions. The average water temperature (colors) and the macronutrient (PO4)
510 concentrations (contours) for model year 197 are compared to the corresponding measured
511 values in World Ocean Atlas (WOA09) within the upper 200m in the northern (60°-66°E and
512 19°-23°N) and southern (60°-66°E and 15°-17°N) part of the region are shown in Fig. 13. In
513 the northern part of the region (see Fig 13a and b), the GFDL model provides a reasonably
514 good estimation of the mean temperature field near the surface, but subsurface temperatures
515 are not as consistent as there is far too little stratification. This is also associated with a very
516 weak nutricline in CM2.6. Variations in isopycnal depth will therefore not lead to big
517 differences in nutrient supply. Figs. 13c and d show the same results for the southern part of
518 the region. Unlike the northern part of the domain, the temperature gradient over these depths
519 is well estimated by CM2.6. While the nutricline is still too weak there is some gradient in
520 nutrients between 80 and 120m.

521 As seen in (Fig. 1d) both the ARGO and WOA09 wintertime mixed layer depth is
522 considerably deeper than that of summer, reaching a maximum of 65m. However, in the
523 northern regions the MLD seems to be too deep in winter, reaching values of 130-150 m. This
524 suggests that the overly deep mixed layer in the northern part of the region may explain both

525 the tendency towards an overly strong winter bloom and the failure of mesoscale eddies in
526 modulating chlorophyll blooms. If we look during the time period where we have eddies E1
527 and E2 (Nov-Dec. year 197, Fig 6c,d) we see shallower mixed layers associated with both
528 eddies.

529 Both the temperature and mixed layer biases in the northern part of the Arabian Sea may
530 result from having too much water from Persian Gulf in this region. This can be seen in the
531 yearly averaged subsurface salinity-density distribution over the region, shown in Figs 13e
532 and f for both WOA09 data and CM2.6 (model year 197), respectively. Fig. 13e shows two
533 separate tongues of salty water, one near the surface and one at the depth of ~300m. These
534 salty water signals are consistent with the seasonal cycle of Persian Gulf outflow as discussed
535 in Ezam et al. (2010). On the other hand, CM2.6 shows one subsurface salty water signal
536 from the northern part, which is deep and strong enough to result in weak stratification in the
537 north to a depth of 250m, as shown in Fig. 13f. These results suggest that a sharp thermocline
538 and nutricline is necessary for eddy activity to modulate the mixing of nutrients to the surface.

539 We test the idea that a sharper thermocline could modulate mixing of nutrients to the surface
540 by looking at the sources of nutrient in the southern part of Arabian Sea where eddy-bloom
541 relationships are seen. Accordingly, the region containing eddy E1 in Fig. 12 is analyzed to
542 determine the physical mechanisms by which nutrient is transported into the surface layer.
543 Fig. 14 contrasts chlorophyll concentration, advection, and diffusion terms for the region from
544 63°-66°E, 15°-18°N over the December of two consecutive CM2.6 years of 197 and 198. In
545 Year 197 we see an eddy associated with a bloom while there is no eddy in year 198 at the
546 same time and the chlorophyll concentrations are much lower. In both years the diffusive flux
547 of nutrient to the top 50m mirrors the chlorophyll. But in 197 it is larger and positive (~10
548 mol/m²/month) in the eddy while the advective flux is actually negative in this region. By
549 contrast in Year 198, there is no cyclonic eddy and the diffusive fluxes are much smaller.

550 The bloom associated with eddies E1 and E2 do not fit with any of the mechanisms
551 highlighted in Gaube et al. (2014). We first consider the mechanism of trapping. Eddy E1 is
552 generated in the ocean interior, not as a result of coastal upwelling. As shown in Fig. 15, the
553 nutrient supply rate ranges between 5 and 8 mmol/m²/month in the eddy. The concentrations
554 in this eddy are only 0.01 μ M (5 mmol/m²) over the top 50 m. It cannot be the case that the
555 nutrients in the eddy can last for several months as a result of “trapping”, there must be a
556 continuous supply. Moreover although eddy E2 shows a horizontal advection signal in

557 November (with a positive ring around the edge in Fig. 12a), the signal in December has the
558 opposite sign. Eddy intensification is also an unlikely mechanism for explaining the blooms,
559 as $d\text{SSH}/dt$ is relatively small (particularly if we track the minimum SSH associated with E1
560 in Fig. 12c or E2 in Fig. 12d). Finally, Ekman pumping signatures in Gaube et al. (2014) have
561 the opposite sign as what is seen in E1 and E2.

562 Our results also contrast with those in Resplandy et al. (2011). The focus in Resplandy et al.
563 (2011) is on the productivity driven by horizontal and vertical advection in summer and
564 mostly vertical advection in winter. This contradicts our finding of a primary diffusive source
565 of nutrient in winter although it is consistent the finding of advective source of nutrients in
566 summer. We point out that in our model, the only two eddies that actually look like what we
567 see in the satellite observations involve enhanced mixing from below. This is a different result
568 from Levy et al. (2014) and Resplandy et al. (2011). Moreover it is not clear whether these
569 papers get the seasonal correlation with SSH or not. Resplandy et al. (2011) do not focus on
570 structures at the eddy scale as they are more concerned with the net impact of eddies.

571

572 To summarize, we hypothesize that

- 573 1. The reason that blooms are found in cyclones in the Arabian Sea during the NEM is that
574 the dominant source of nutrients to the surface, i.e. mixing (Barimalala et al., 2013;
575 Kawamiya and Oschlies, 2003) is concentrated there.
- 576 2. Interannual variability in wintertime blooms in the Northwest Arabian Sea is controlled by
577 the combined presence of these eddies and strength of wintertime cooling.
- 578 3. Excessive mixing (resulting in too weak a thermocline) prevents mixing from being
579 modulated by eddies in the model except occasionally in the southern part of our region. In
580 the real world the modulation of mixing seen in Fig. 14 extends into the Northwest Arabian
581 Sea and the Gulf of Oman.

582 **5 Conclusions**

583 Our analysis of bloom variability in the northwestern Arabian Sea and Gulf of Oman has
584 illustrated a set of both similar and dissimilar descriptive features between satellites and
585 among a suite of models and explored the various mechanisms involved. Satellite analyses
586 verified the existence of two blooms, the stronger one associated with the Southwest monsoon

587 and the weaker one associated with the Northeast Monsoon as also shown by Madhupratap et
588 al. (1996), Kawamiya and Oschlies (2003), Murtugudde et al. (2007), and Al-Azri et al.
589 (2010). We demonstrate a pronounced anti-correlation between SSHA and chlorophyll
590 blooms in during certain times in northern winter but a much weaker relationship in other
591 months (typically northern summer) with the relationship disappearing as the blooms vanish
592 in the months of April and May (northern spring). While the depth of thermocline and
593 nutricline and also stratification are affecting the convection during the Northeast Monsoon
594 (Dickey et al., 1998; Kumar et al., 2001; Wiggert et al., 2002), we show that a thin
595 nutricline/thermocline and a strong stratification are also required to enable cold eddies to
596 bring nutrients to euphotic zone and develop phytoplankton blooms. During the wintertime
597 monsoon, while both cooling in the winter and eddies control the blooms, variability in bloom
598 location will arise from variability in the location of eddies, and so may not be predictable. In
599 contrast, during the Southwest Monsoon the dominant upwelling associated with the intense
600 environmental forcing supersedes the effect of eddies and the activity of the cold eddies is not
601 pronounced.

602 Understanding of this phenomenon has been sought using three different 3D ocean-
603 atmosphere models, including a CORE-forced ocean with the TOPAZ biogeochemistry, a
604 coupled model with the TOPAZ biogeochemistry and CM2.6. Because the coarse models with
605 TOPAZ are not able to capture eddies and the interannual variability, CM2.6 (miniBLING), a
606 eddy-resolving high resolution model, was also considered for simulating the spatial and
607 temporal changes of the bloom in the region. This model simulates the two blooms seen in the
608 data and shows that the nutrients driving the northern summer bloom are supplied by
609 advection while those driving the wintertime bloom are supplied by vertical diffusion.
610 However, this model is unable to simulate the seasonal relationship observed in the satellite
611 products between blooms and sea surface height. Although there is some anti-correlation, it
612 tends to be associated with larger spatial scales and not really related to eddies. Instead,
613 eddies in the model usually wrap the chlorophyll around themselves, producing high
614 chlorophyll concentrations around their edges and not at their centers. Comparing the model
615 results to field measurements (WOA09) showed that the model does not account for the
616 strong thermocline and nutricline in the northern part of the region. In the wintertime, this
617 leads to excessive convective supply of nutrients and too strong of a bloom. However, for a
618 few cases eddies with a bloom at the center are tracked in the southern part of the domain. In
619 this region consistency is observed between the model results and the field data. Analysis of

620 the term balances in mixed layer show that eddies in this region modulate the diffusive supply
621 of nutrients. We suggest that what happens in the model in the Southern Arabian Sea actually
622 describes the Arabian Sea as a whole according to the observations and the field data. The
623 model misses the eddy signal in the north because it lacks a thin nutricline, motions of which
624 will lead to differences in nutrient supply. In the real world, eddies modulate the diffusive
625 supply of nutrients during the wintertime and there is more mixing in the eddy centers along
626 with the diffusive supply provided by the cooling in the wintertime. Accordingly, there is a
627 potential to improve the numerical models by better simulating the Persian Gulf Outflow to
628 produce a sharper thermocline, allowing more realistic nutrient supply.

629 It is worth noting that regional models, (such as Resplandy et al. (2011)) do have the potential
630 to better simulate the hydrography of the Northern Arabian Sea. Because such models are
631 very tightly constrained through “sponges” that restore hydrography at the boundaries, they
632 may not have the problems that global models do at representing the effects of overflows that
633 they do not properly simulate. However, such models cannot by themselves simulate the
634 effects of changing climate, which in turn changes the boundary conditions. For this reason,
635 global models must still be used for projection, making it important to identify the reasons
636 that they are not going to work.

637

638 **Acknowledgements**

639 The authors thank Eric Galbraith, Shahabeddin Torabian, Grace Kim, Carlos del Castillo, and
640 Jeremy Wardell for useful discussions. We also thank Rick Slater and Whit Anderson for
641 their support of the model simulations.

642

643

644 **References**

645 Adcroft, A., Campin, J.-M., Hill, C. and Marshall, J.: Implementation of an Atmosphere–
646 Ocean General Circulation Model on the Expanded Spherical Cube, *Mon. Weather Rev.*,
647 132(12), 2845–2863, doi:10.1175/MWR2823.1, 2004.

648 Al-Azri, A. R., Piontkovski, S. a., Al-Hashmi, K. a., Goes, J. I., Gomes, H. D. R. and Glibert,
649 P. M.: Mesoscale and Nutrient Conditions Associated with the Massive 2008 *Cochlodinium*
650 *polykrikoides* Bloom in the Sea of Oman/Arabian Gulf, *Estuaries and Coasts*,
651 doi:10.1007/s12237-013-9693-1, 2013.

652 Al-Azri, A. R., Piontkovski, S. A., Al-Hashmi, K. A., Goes, J. I. and Gomes, H. R.:
653 Chlorophyll a as a measure of seasonal coupling between phytoplankton and the monsoon
654 periods in the Gulf of Oman, *Aquat. Ecol.*, 44(2), 449–461, doi:10.1007/s10452-009-9303-2,
655 2010.

656 Anderson, D. M. and Prell, W. L.: A 300 KYR Record of Upwelling Off Oman During the
657 Late Quaternary: Evidence of the Asian Southwest Monsoon, *Paleoceanography*, 8(2), 193–
658 208, 1993.

659 Armstrong, R. A., Lee, C., Hedges, J. I., Honjo, S. and Wakeham, S. G.: A new, mechanistic
660 model for organic carbon fluxes in the ocean based on the quantitative association of POC
661 with ballast minerals, *Deep. Res. Part II Top. Stud. Oceanogr.*, 49(1-3), 219–236,
662 doi:10.1016/S0967-0645(01)00101-1, 2002.

663 Banse, K. and McClain, C. R.: Winter blooms of phytoplankton in the Arabian Sea as
664 observed by the Coastal Zone Color Scanner, *Mar Ecol Prog Ser*, 34, 201–211, 1986.

665 Barimalala, R., Bracco, A., Kucharski, F., McCreary, J. P. and Crise, A.: Arabian Sea
666 ecosystem responses to the South Tropical Atlantic teleconnection, *J. Mar. Syst.*, 117-118,
667 14–30, doi:10.1016/j.jmarsys.2013.03.002, 2013.

668 Bartolacci, D. M. and Luther, M. E.: Patterns of co-variability between physical and
669 biological parameters in the Arabian Sea, *Deep Sea Res. Part II Top. Stud. Oceanogr.*, 46(8-
670 9), 1933–1964, doi:10.1016/S0967-0645(99)00049-1, 1999.

671 Behrenfeld, M. J.: Abandoning Sverdrup’s Critical Depth Hypothesis on phytoplankton
672 blooms, *Ecology*, 91(4), 977–989, doi:10.1890/09-1207.1, 2010.

673 Behrenfeld, M. J., Boss, E., Siegel, D. A. and Shea, D. M.: Carbon-based ocean productivity
674 and phytoplankton physiology from space, *Global Biogeochem. Cycles*, 19(1), 1–14,
675 doi:10.1029/2004GB002299, 2005.

676 Bryan, K. and Lewis, L. J.: A Water Mass Moel of the World Ocean, , 84(8), 2503, 1979.

677 Danabasoglu, G., Large, W. G., Tribbia, J. J., Gent, P. R., Briegleb, B. P. and McWilliams, J.
678 C.: Diurnal coupling in the tropical oceans of CCSM3, *J. Clim.*, 19(11), 2347–2365,
679 doi:10.1175/JCLI3739.1, 2006.

680 Delworth, T. L., Broccoli, A. J., Rosati, A., Stouffer, R. J., Balaji, V., Beesley, J. A., Cooke,
 681 W. F., Dixon, K. W., Dunne, J., Dunne, K. A., Durachta, J. W., Findell, K. L., Ginoux, P.,
 682 Gnanadesikan, A., Gordon, C. T., Griffies, S. M., Gudgel, R., Harrison, M. J., Held, I. M.,
 683 Hemler, R. S., Horowitz, L. W., Klein, S. A., Knutson, T. R., Kushner, P. J., Langenhorst, A.
 684 R., Lee, H. C., Lin, S. J., Lu, J., Malyshev, S. L., Milly, P. C. D., Ramaswamy, V., Russell, J.,
 685 Schwarzkopf, M. D., Shevliakova, E., Sirutis, J. J., Spelman, M. J., Stern, W. F., Winton, M.,
 686 Wittenberg, A. T., Wyman, B., Zeng, F. and Zhang, R.: GFDL's CM2 global coupled climate
 687 models. Part I: Formulation and simulation characteristics, *J. Clim.*, 19(5), 643–674,
 688 doi:10.1175/JCLI3629.1, 2006.

689 Delworth, T. L., Rosati, A., Anderson, W., Adcroft, A. J., Balaji, V., Benson, R., Dixon, K.,
 690 Griffies, S. M., Lee, H.-C., Pacanowski, R. C., Vecchi, G. A., Wittenberg, A. T., Zeng, F. and
 691 Zhang, R.: Simulated Climate and Climate Change in the GFDL CM2.5 High-Resolution
 692 Coupled Climate Model, *J. Clim.*, 25(8), 2755–2781, doi:10.1175/JCLI-D-11-00316.1, 2012.

693 Dickey, T., Marra, J., Sigurdson, D. E., Weller, R. A., Kinkade, C. S., Zedler, S. E., Wiggert,
 694 J. D. and Langdon, C.: Seasonal variability of bio-optical and physical properties in the
 695 Arabian Sea : October 1994 — October 1995, *Deep. Res. II*, 45(October 1994), 2001–2025,
 696 1998.

697 Dunne, J., Gnanadesikan, A., Sarmiento, J. L. and Slater, R. D.: Technical description of the
 698 prototype version (v0) of Tracers Of Phytoplankton with Allometric Zooplankton (TOPAZ)
 699 ocean biogeochemical model as used in the Princeton IFMIP* model, *Biogeosciences Suppl.*,
 700 7(1), 3593, doi:10.5194/bg-7-3593-2010, 2010.

701 Dunne, J. P., John, J. G., Adcroft, A. J., Griffies, S. M. and Hallberg, R. W.: GFDL's ESM2
 702 Global Coupled Climate-Carbon Earth System Models. Part I: Physical Formulation and
 703 Baseline Simulation Characteristics, *J. Clim.*, 25, 6646–6665,
 704 doi:<http://dx.doi.org/10.1175/JCLI-D-11-00560.1>, 2012.

705 Dunne, J. P., John, J. G., Shevliakova, S., Stouffer, R. J., Krasting, J. P., Malyshev, S. L.,
 706 Milly, P. C. D., Sentman, L. T., Adcroft, A. J., Cooke, W., Dunne, K. A., Griffies, S. M.,
 707 Hallberg, R. W., Harrison, M. J., Levy, H., Wittenberg, A. T., Phillips, P. J. and Zadeh, N.:
 708 GFDL's ESM2 global coupled climate-carbon earth system models. Part II: Carbon system
 709 formulation and baseline simulation characteristics, *J. Clim.*, 26(7), 2247–2267,
 710 doi:10.1175/JCLI-D-12-00150.1, 2013.

711 Dunne, J. P., Sarmiento, J. L. and Gnanadesikan, A.: A synthesis of global particle export
 712 from the surface ocean and cycling through the ocean interior and on the seafloor, *Global*
 713 *Biogeochem. Cycles*, 21(4), 1–16, doi:10.1029/2006GB002907, 2007.

714 Ezam, M., Bidokhti, A. A. and Javid, a. H.: Numerical simulations of spreading of the
 715 Persian Gulf outflow into the Oman Sea, *Ocean Sci.*, 6(4), 887–900, doi:10.5194/os-6-887-
 716 2010, 2010.

717 Fischer, A. S., Weller, R. A., Rudnick, D. L., Eriksen, C. C., Lee, C. M., Brink, K. H., Fox, C.

718 A. and Leben, R. R.: Mesoscale eddies, coastal upwelling, and the upper-ocean heat budget in
719 the Arabian Sea, *Deep Sea Res. Part II Top. Stud. Oceanogr.*, 49(12), 2231–2264,
720 doi:10.1016/S0967-0645(02)00036-X, 2002.

721 Fox-Kemper, B., Ferrari, R. and Hallberg, R.: Parameterization of Mixed Layer Eddies. Part
722 I: Theory and Diagnosis, *J. Phys. Oceanogr.*, 38(6), 1145–1165, doi:10.1175/2007JPO3792.1,
723 2008.

724 Galbraith, E. D., Dunne, J. P., Gnanadesikan, A., Richard, D., Sarmiento, J. L., Dufour, C. O.,
725 Gregory, F., Bianchi, D., Claret, M., Rodgers, K. B. and Sedigh Marvasti, S.: Parameterized
726 complexity for simulating realistic biogeochemistry with few tracers in Earth System Models,
727 *J. Adv. Model. Earth Syst.*, (Sumbitted), 2015.

728 Galbraith, E., Gnanadesikan, A., Dunne, J. and Hiscock, M.: Regional impacts of iron-light
729 colimitation in a global biogeochemical model., *Biogeosciences*, 7, 1043–1064, 2010.

730 Gaube, P., McGillicuddy, D., Chelton, D., Behrenfeld, M. J. and Strutton, P.: Regional
731 variations in the influence of mesoscale eddies on near-surface chlorophyll Peter, J. *Geophys.*
732 *Res. Ocean.*, 119, 8195–8220, doi:10.1002/2014JC010111. Received, 2014.

733 Gnanadesikan, A., Dixon, K. W., Griffies, S. M., Balaji, V., Barreiro, M., Beesley, J. A.,
734 Cooke, W. F., Delworth, T. L., Gerdes, R., Harrison, M. J., Held, I. M., Hurlin, W. J., Lee, H.
735 C., Liang, Z., Nong, G., Pacanowski, R. C., Rosati, A., Russell, J., Samuels, B. L., Song, Q.,
736 Spelman, M. J., Stouffer, R. J., Sweeney, C. O., Vecchi, G., Winton, M., Wittenberg, A. T.,
737 Zeng, F., Zhang, R. and Dunne, J. P.: GFDL's CM2 global coupled climate models. Part II:
738 The baseline ocean simulation, *J. Clim.*, 19(5), 675–697, doi:10.1175/JCLI3630.1, 2006.

739 Gnanadesikan, A., Dunne, J. P. and John, J.: What ocean biogeochemical models can tell us
740 about bottom-up control of ecosystem variability, *ICES J. Mar. Sci.*, 68(6), 1030–1044,
741 doi:10.1093/icesjms/fsr068, 2011.

742 Gnanadesikan, A., Dunne, J. P. and Msadek, R.: Connecting Atlantic temperature variability
743 and biological cycling in two earth system models, *J. Mar. Syst.*, 133, 39–54,
744 doi:10.1016/j.jmarsys.2013.10.003, 2014.

745 Goes, J. I., Thoppil, P. G., Gomes, H. D. R. and Fasullo, J. T.: Warming of the Eurasian
746 landmass is making the Arabian Sea more productive., *Science*, 308(5721), 545–547,
747 doi:10.1126/science.1106610, 2005.

748 Gomes, R., Goes, J. I., Matondkar, S. G. P., Parab, S. G., Al-azri, A. R. N. and Thoppil, P. G.:
749 Deep-Sea Research I Blooms of *Noctiluca miliaris* in the Arabian Sea — An in situ and
750 satellite study, *Deep Sea Res. Part I Oceanogr. Res. Pap.*, 55, 751–765,
751 doi:10.1016/j.dsr.2008.03.003, 2008.

752 Griffies, S. M., Biastoch, A., Böning, C., Bryan, F., Danabasoglu, G., Chassignet, E. P.,
753 England, M. H., Gerdes, R., Haak, H., Hallberg, R. W., Hazeleger, W., Jungclaus, J., Large,
754 W. G., Madec, G., Pirani, A., Samuels, B. L., Scheinert, M., Gupta, A. Sen, Severijns, C. A.,

755 Simmons, H. L., Treguier, A. M., Winton, M., Yeager, S. and Yin, J.: Coordinated Ocean-ice
756 Reference Experiments (COREs), Ocean Model., 26(1-2), 1–46,
757 doi:10.1016/j.ocemod.2008.08.007, 2009.

758 Griffies, S. M., Gnanadesikan, a., Dixon, K. W., Dunne, J. P., Gerdes, R., Harrison, M. J.,
759 Rosati, a., Russell, J. L., Samuels, B. L., Spelman, M. J., Winton, M. and Zhang, R.:
760 Formulation of an ocean model for global climate simulations, Ocean Sci. Discuss., 2(3),
761 165–246, doi:10.5194/osd-2-165-2005, 2005.

762 Hamzehei, S. and Bidokhti, A.: Red tide monitoring in the Persian Gulf and Gulf of Oman
763 using MODIS sensor data., Tech. J., 1100–1107, 2013.

764 Honjo, S., Dymond, J., Prell, W. and Ittekkot, V.: Monsoon-controlled export fluxes to the
765 interior of the Arabian Sea, Deep. Res. II, 46(1999), 1859–1902, 2000.

766 Kawamiya, M. and Oschlies, A.: An eddy-permitting , coupled ecosystem-circulation model
767 of the Arabian Sea : comparison with observations, J. Mar. Syst., 38, 221–257, 2003.

768 Klaas, C. and Archer, D. E.: Association of sinking organic matter with various types of
769 mineral ballast in the deep sea: Implications for the rain ratio, Global Biogeochem. Cycles,
770 16(4), 1116, doi:10.1029/2001GB001765, 2002.

771 Kostadinov, T. S., Siegel, D. A. and Maritorena, S.: Retrieval of the particle size distribution
772 from satellite ocean color observations, J. Geophys. Res., 114(C9), C09015,
773 doi:10.1029/2009JC005303, 2009.

774 Kumar, S. P., Ramaiah, N., Gauns, M., Sarma, V. V. S. S., Muraleedharan, P. M.,
775 Raghukumar, S., Kumar, M. D. and Madhupratap, M.: Physical forcing of biological
776 productivity in the Northern Arabian Sea during the Northeast Monsoon, Deep. Res. II, 48,
777 1115–1126, 2001.

778 Large, W. G., McWilliams, J. C. and Doney, S. C.: Oceanic vertical mixing: A review and a
779 model with a nonlocal boundary layer parameterization, Rev. Geophys., 32(4), 363,
780 doi:10.1029/94RG01872, 1994.

781 Levy, M., Resplandy, L. and Lengaigne, M.: Oceanicmesoscale turbulence drives large
782 biogeochemical interannual variability atmiddle and high latitudes, Geophys. Res. Lett.,
783 41(7), 2467–2474, doi:10.1002/2014GL059608, 2014.

784 Levy, M., Shankar, D., Andre, J., Shenoi, S. S. C., Durand, F. and Montegut, C. D. B.: Basin-
785 wide seasonal evolution of the Indian Ocean ' s phytoplankton blooms, J. Geophys. Res.,
786 112(C12014), 1–14, 2007.

787 Madhupratap, M., Kumar, S., Bhattathiri, P., Kumar, M., Raghukumar, S., Nair, K. and
788 Ramaiah, N.: Mechanism of the biological response to winter cooling in the northeastern
789 Arabian Sea, Nature, 384(12), 549–552, 1996.

790 Maritorena, S., Siegel, D. a and Peterson, A. R.: Optimization of a semianalytical ocean color

791 model for global-scale applications., *Appl. Opt.*, 41(15), 2705–14, 2002.

792 McGillicuddy, D., Kosnyrev, V., Ryan, J. and Yoder, J.: Covariation of mesoscale ocean
793 color and sea-surface temperature patterns in the Sargasso Sea, *Deep. Res. II*, 48, 1823–1836,
794 2001.

795 Murtugudde, R., Seager, R. and Thoppil, P.: Arabian Sea response to monsoon variations,
796 *Paleoceanography*, 22(4), 1–17, doi:10.1029/2007PA001467, 2007.

797 Naqvi, S. W. A., Moffett, J. W., Gauns, M. U., Narvekar, P. V, Pratihary, A. K., Naik, H.,
798 Shenoy, D. M., Jayakumar, D. A., Goepfer, T. J., Patra, P. K., Al-Azri, A. and Ahmed, S. I.:
799 The Arabian Sea as a high-nutrient , low-chlorophyll region during the late Southwest
800 Monsoon, *Biogeosciences*, 7, 2091–2100, doi:10.5194/bg-7-2091-2010, 2010.

801 Piontkovski, S., Al-Azri, A. and Al-Hashmi, K.: Seasonal and interannual variability of
802 chlorophyll- a in the Gulf of Oman compared to the open Arabian Sea regions, *Int. J. Remote
803 Sens.*, 32(22), 7703–7715, doi:10.1080/01431161.2010.527393, 2011.

804 Piontkovski, S., Al-Gheilani, H., Jupp, B., Al-Azri, A. and Al-Hashmi, K.: Interannual
805 Changes in the Sea of Oman Ecosystem., *Open Mar. Biol. J.*, 6, 38–52, 2012.

806 Resplandy, L., Lévy, M., Madec, G., Pous, S., Aumont, O. and Kumar, D.: Contribution of
807 mesoscale processes to nutrient budgets in the Arabian Sea, *J. Geophys. Res. Ocean.*, 116(11),
808 1–24, doi:10.1029/2011JC007006, 2011.

809 Richlen, M. L., Morton, S. L., Jamali, E. A., Rajan, A. and Anderson, D. M.: The catastrophic
810 2008–2009 red tide in the Arabian gulf region, with observations on the identification and
811 phylogeny of the fish-killing dinoflagellate *Cochlodinium polykrikoides*, *Harmful Algae*,
812 9(2), 163–172, doi:10.1016/j.hal.2009.08.013, 2010.

813 Sarma, Y. V. B., Al-Hashmi, K. and Smith, L. S.: Sea Surface Warming and its Implications
814 for Harmful Algal Blooms off Oman, *Int. J. Mar. Sci.*, 3(8), 65–71,
815 doi:10.5376/ijms.2013.03.0008, 2013.

816 Shalapyonok, A., Olson, R. J. and Shalapyonok, L. S.: Arabian Sea phytoplankton during
817 Southwest and Northeast Monsoons 1995 : composition , size structure and biomass from
818 individual cell properties measured by flow cytometry, *Deep. Res. II*, 48, 1231–1261, 2001.

819 Simmons, H. L., Jayne, S. R., St. Laurent, L. C. and Weaver, A. J.: Tidally driven mixing in a
820 numerical model of the ocean general circulation, *Ocean Model.*, 6(3-4), 245–263,
821 doi:10.1016/S1463-5003(03)00011-8, 2004.

822 Stacey, M. W., Pond, S. and Nowak, Z. P.: A Numerical Model of the Circulation in Knight
823 Inlet, British Columbia, Canada, *J. Phys. Oceanogr.*, 25(6), 1037–1062, doi:10.1175/1520-
824 0485(1995)025<1037:ANMOTC>2.0.CO;2, 1995.

825 Tang, D., Kawamura, H. and Luis, A. J.: Short-term variability of phytoplankton blooms
826 associated with a cold eddy in the northwestern Arabian Sea, *Remote Sens. Environ.*, 81, 82–

827 89, 2002.

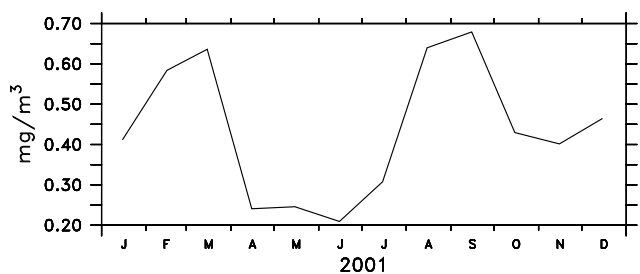
828 Veldhuis, M. J. W., Kraay, G. W., Van Bleijswijk, J. D. L. and Baars, M. A.: Seasonal and
829 spatial variability in phytoplankton biomass , productivity and growth in the northwestern
830 Indian Ocean: the southwest and northeast monsoon , 1992-1993, Deep Sea Res. Part I,
831 44(3), 425–449, 1997.

832 Wang, D. and Zhao, H.: Estimation of phytoplankton responses to Hurricane Gonu over the
833 Arabian Sea based on ocean color data, Sensors, 4878–4893, doi:10.3390/s8084878, 2008.

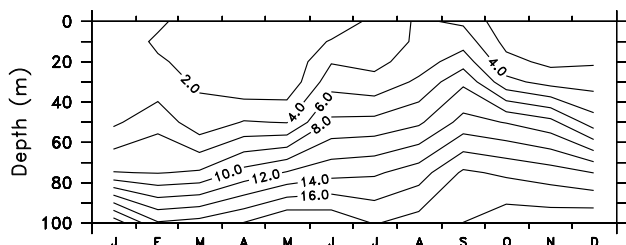
834 Wiggert, J. D., Murtugudde, R. G. and Christian, J. R.: Annual ecosystem variability in the
835 tropical Indian Ocean: Results of a coupled bio-physical ocean general circulation model,
836 Deep. Res. II, 53, 644–676, doi:10.1016/j.dsr2.2006.01.027, 2006.

837 Wiggert, J. D., Murtugudde, R. G. and McClain, C. R.: Processes controlling interannual
838 variations in wintertime (Northeast Monsoon) primary productivity in the central Arabian
839 Sea, Deep. Res. II, 49, 2319–2343, 2002.

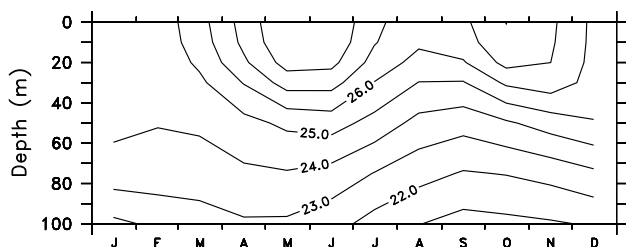
840



(A) GSM Chlorophyll a (mg/m³)

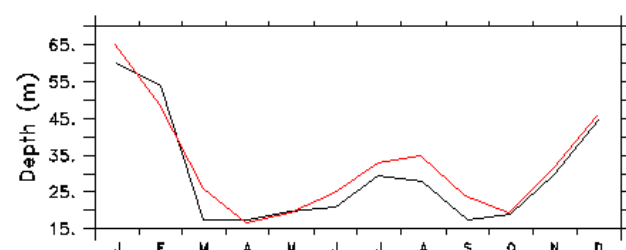


(B) WOA09: Nitrate (micromoles/l)



(C) WOA09: Water Temperature (degrees C)

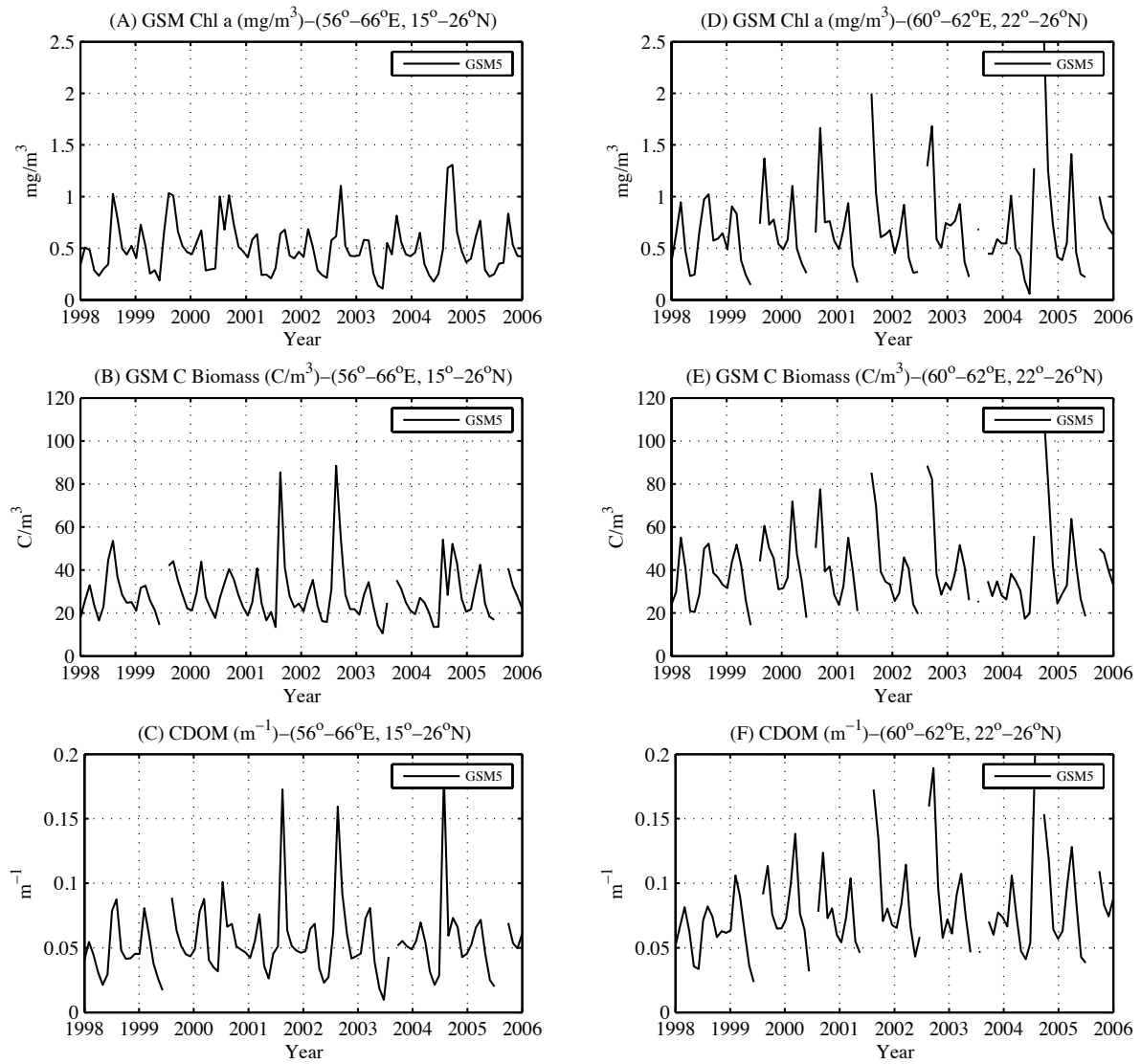
841



842

(D) MLD-WOA(Black) , MLD-Argo(Red)

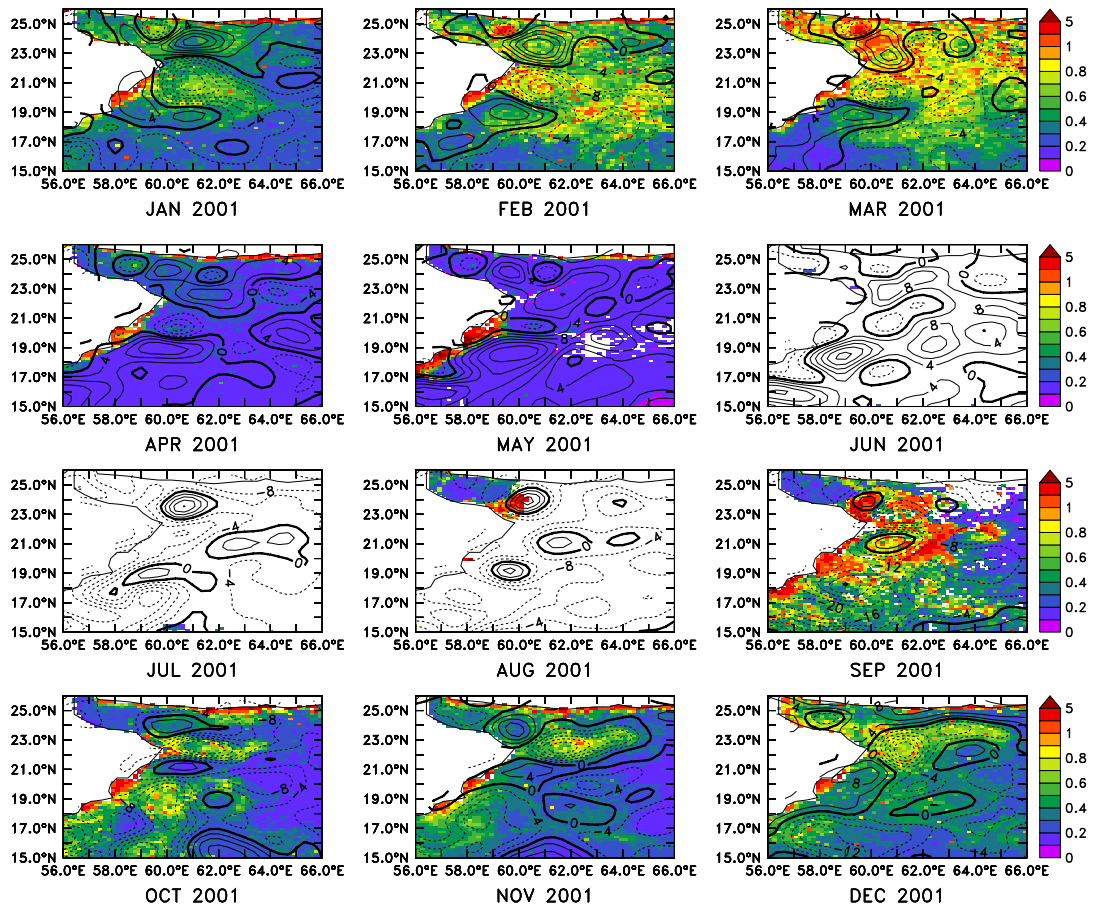
843 Figure 1. Monthly average for region from 56°E-66°E, 15°N-26°N: (a) Surface chlorophyll-a
 844 in 2001 (SeaWiFS); (b) Nitrate (WOA09) over top 100m; (c) Temperature over top 100m; (d)
 845 WOA09 seasonal mixed layer depth in meters.



846

847 Figure 2. Monthly variation of organic matter in satellite data between 1998 and 2005 within
 848 56°-66°E, 15°-26°N (large region); and 60°-62°E, 22°-26°N (small region): (a) and (d)
 849 chlorophyll; (b) and (e) particulate backscatter; (c) and (f) CDOM.

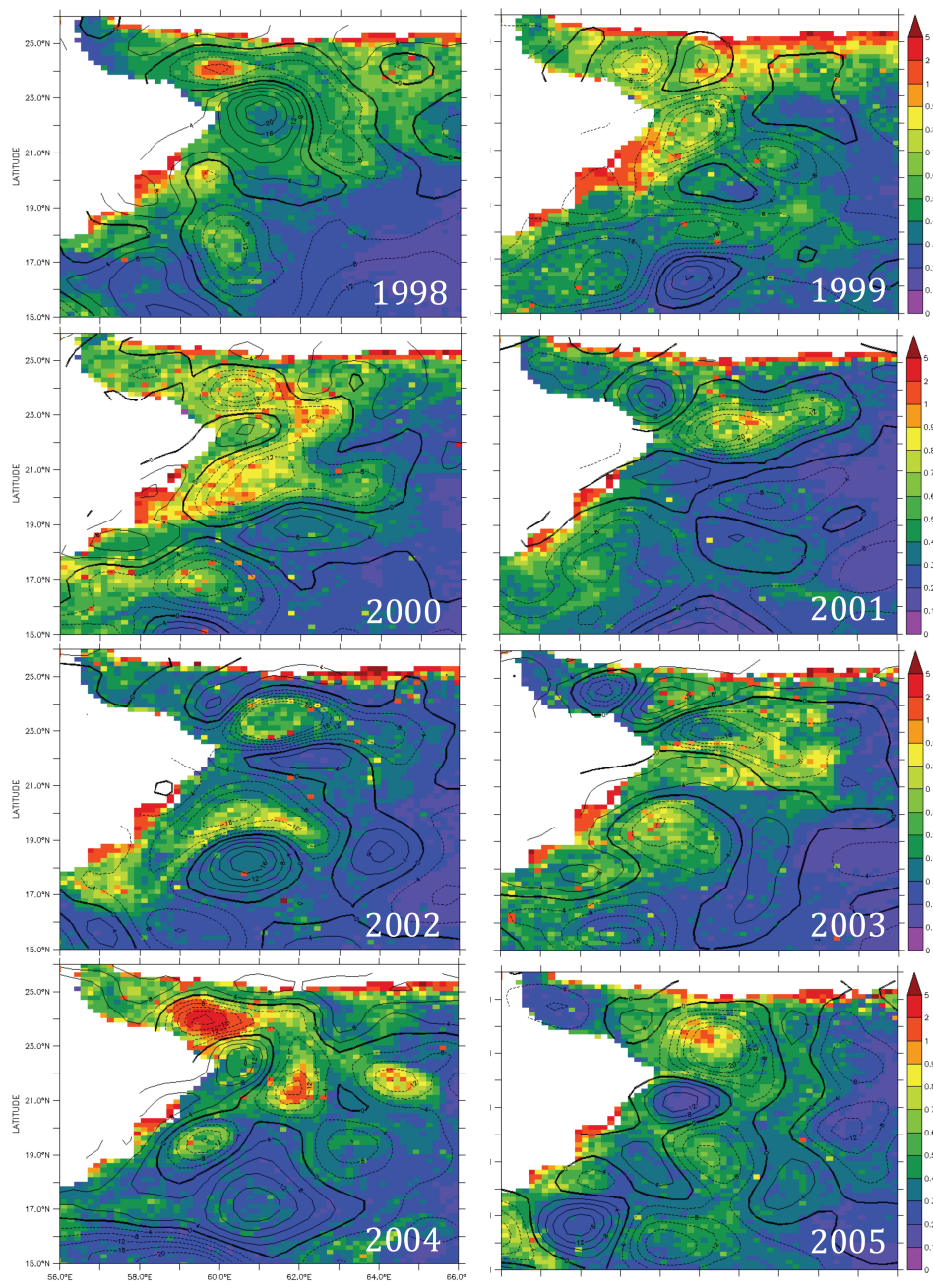
850

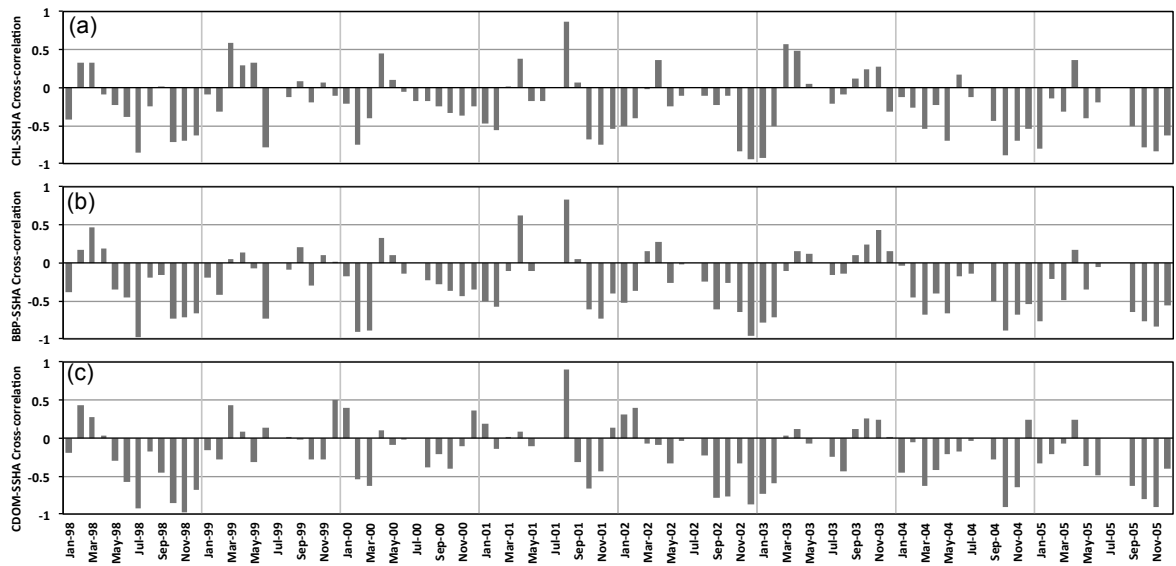


851

852 Figure 3. Chlorophyll-a in mg/m^3 (colors) and Sea-Surface height anomaly (SSHA, contours)
 853 in meter in Gulf of Oman over the course of 2001.

854

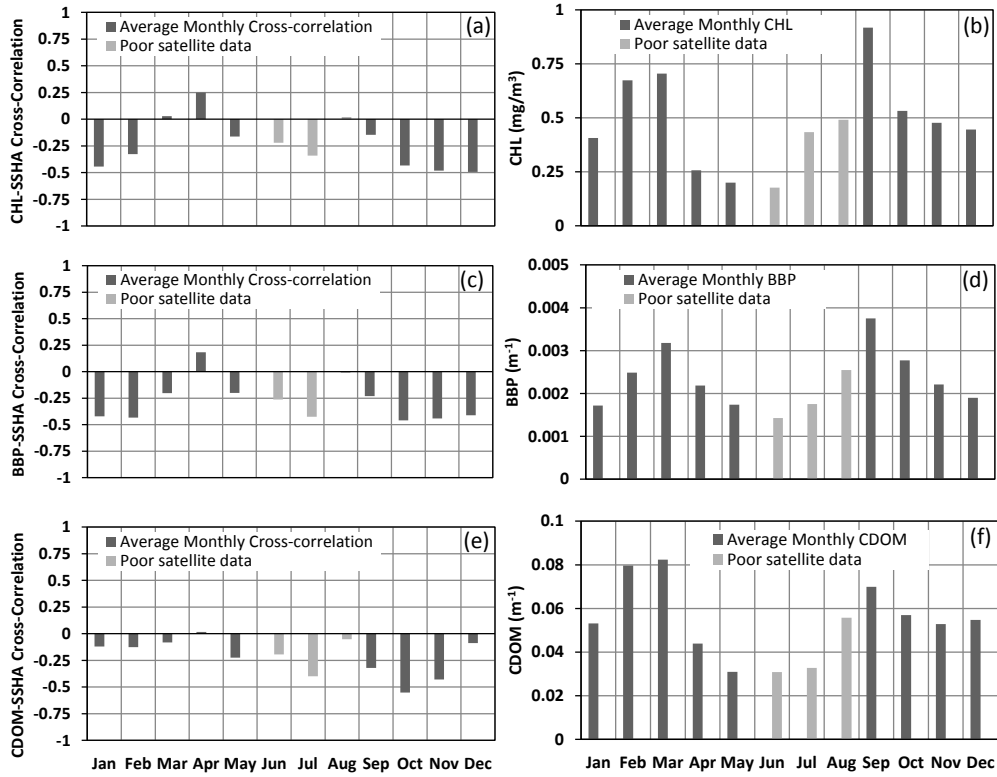




859

860 Figure 5. Monthly chlorophyll-SSHA cross-correlation between 1998 and 2005 within 56° -
 861 66° E and 15° - 26° N. (a) chlorophyll; (b) BBP; (c) CDOM.

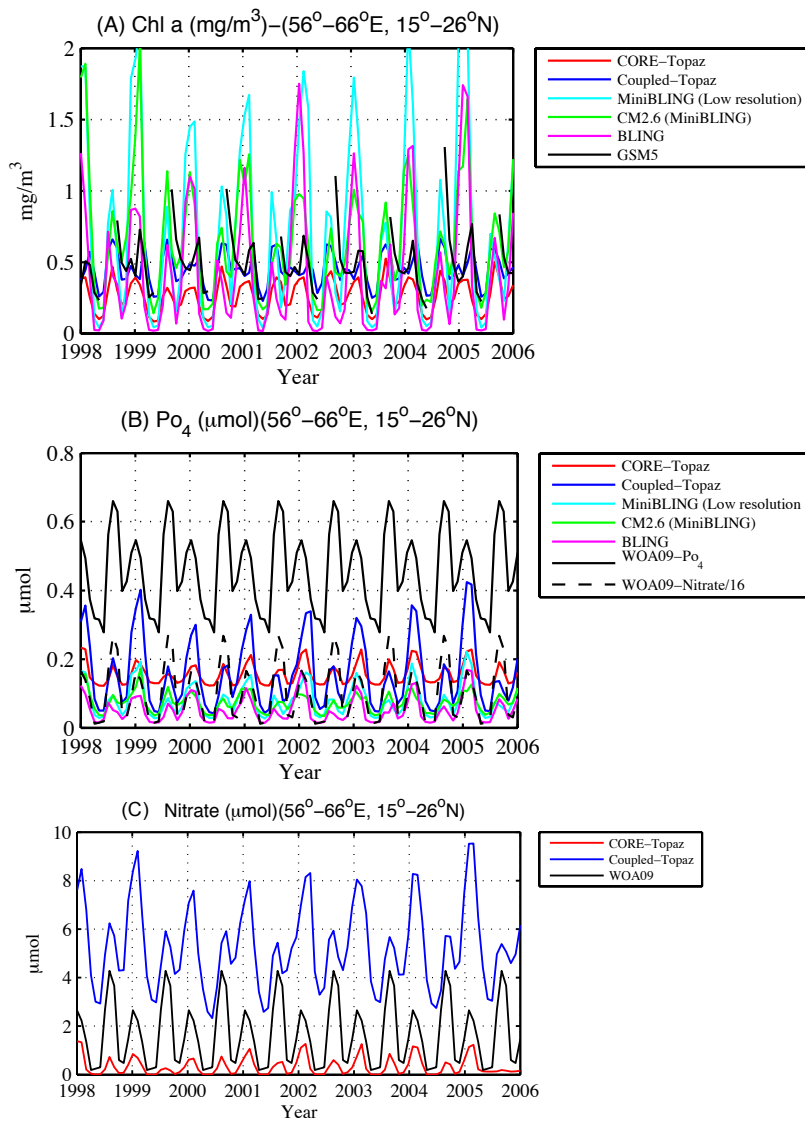
862



863

864 Figure 6. Average monthly cross-correlation with SSHA and average monthly values between
 865 1998 and 2005 within 56° - 66° E and 15° - 26° N: (a, b) chlorophyll; (c, d) backscatter; (e, f)
 866 CDOM.

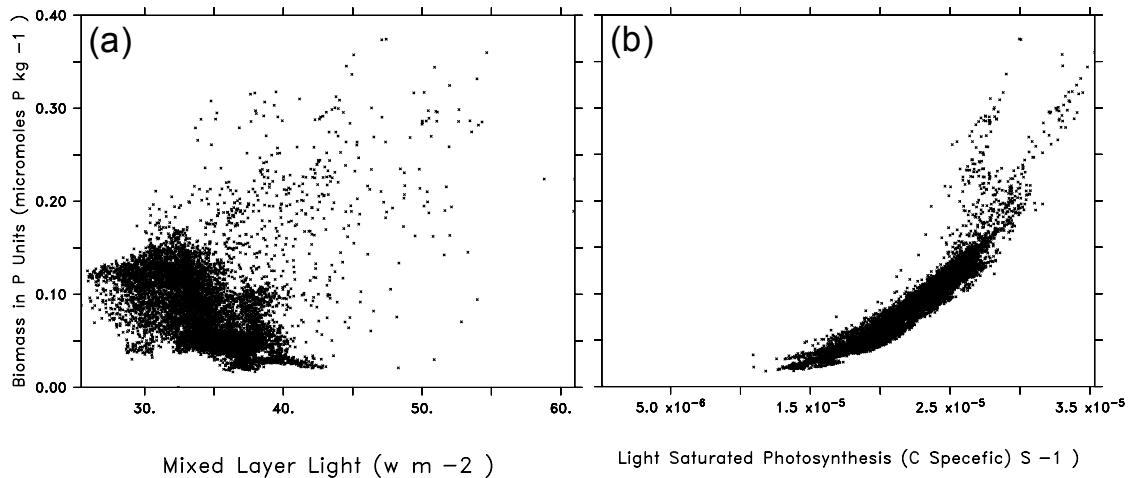
867



868

869 Figure 7. Monthly variation of organic matter in satellite data between 1998 and 2005 and
 870 GFDL models (8 characteristic years) within 56–66E, 15–26N: (a) chlorophyll from GFDL
 871 models and GSM5 algorithm. (b) PO_4 from the BLING and miniBLING simulations, $\text{NO}_3/16$
 872 from the TOPAZ simulations and observed PO_4 from WOA09. (c) NO_3 from the TOPAZ
 873 simulations and observed NO_3 from WOA09.

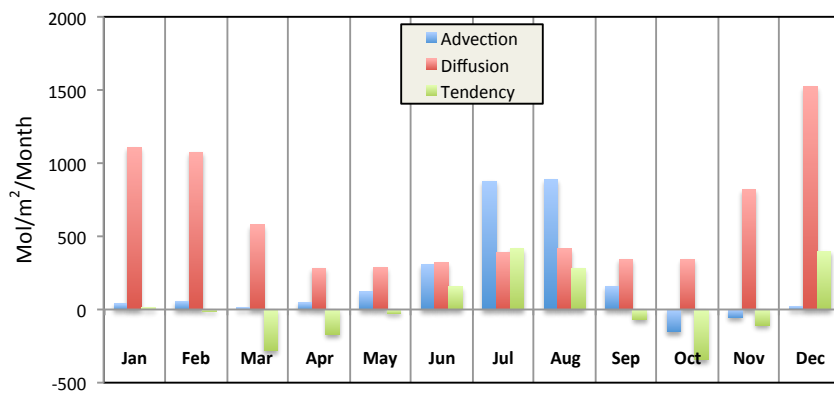
874



875

876 Figure 8. Modeled biomass in CM2.6 in P units (mol P kg⁻¹) versus: (a) Mixed layer
 877 irradiance (Wm⁻²); (b) Light-Saturated photosynthesis rate (carbon specific) (s⁻¹) 56°-66°E,
 878 15°-26°N for January of year 195. In the model, biomass is a function of the growth rate
 879 smoothed over several days, and the light-saturated photosynthesis rate indicates the extent to
 880 which this growth rate is controlled by nutrient limitation.

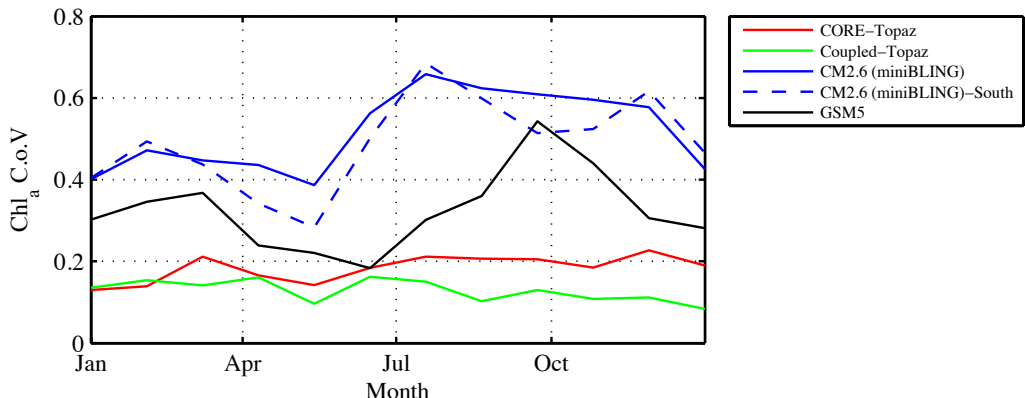
881



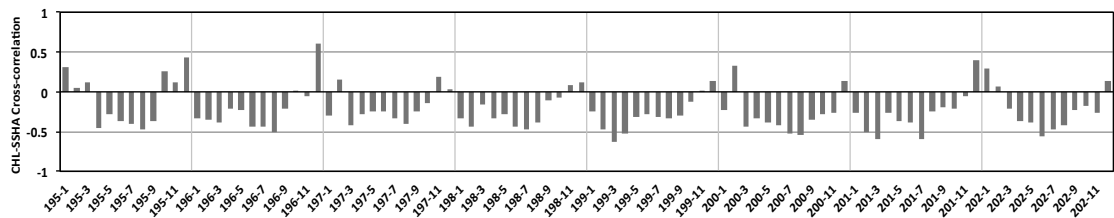
882

883 Figure 9. PO₄ Advection, diffusion and tendency flux from the CM2.6 model over the whole
 884 region averaged over top 50 m (56°-66°E, 15°-26°N).

885

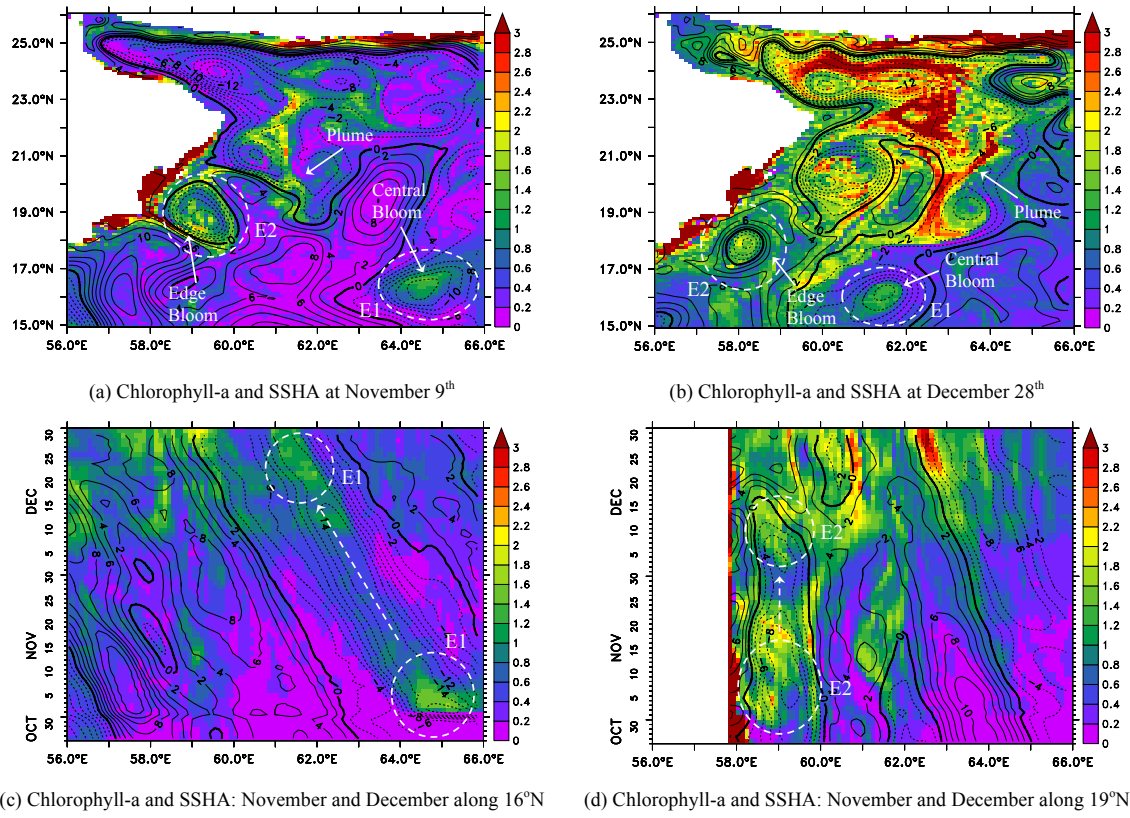


888 Figure 10. Average monthly coefficient of variation of Chlorophyll a in satellite data between
 889 1998 and 2005 and GFDL models (eight characteristics years) within (56° – 66° E, 15° – 26° N)
 890 for the satellite data (black), CORE-TOPAZ (red), COUPLED-TOPAZ (green) and CM2.6
 891 model with miniBLING (blue) and within the south region (56° – 66° E, 15° – 19° N) for CM2.6
 892 (miniBLING, dashed blue).



895

896 Figure 11. CM2.6 monthly Chlorophyll-SSHA cross-correlation over 8 years within 56° - 66° E
 897 and 15° - 26° N.



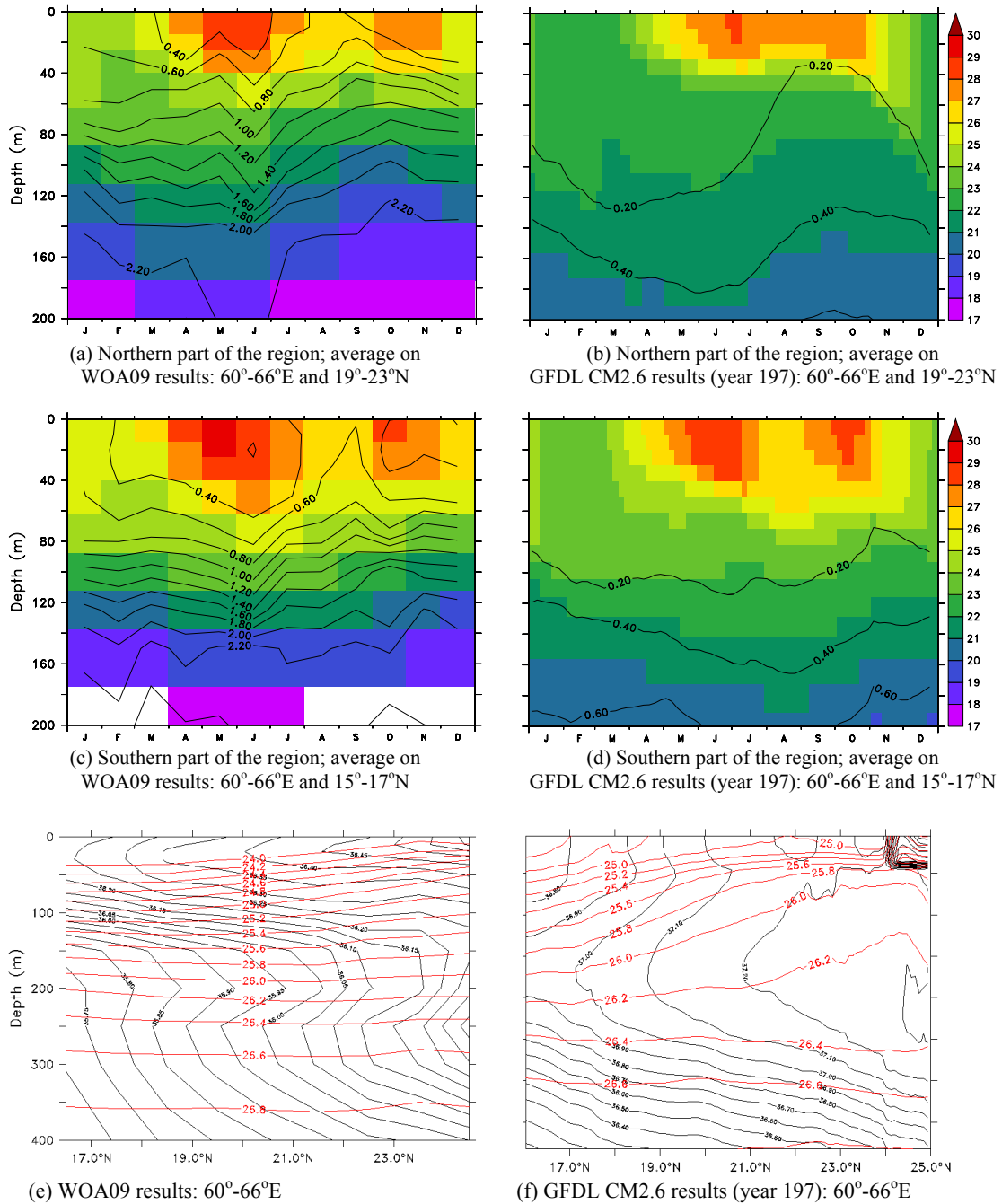
898

899 Figure 12. CM2.6 (miniBLING) Surface chlorophyll-a concentration and sea surface height
900 anomaly (SSHA) November and December during a year where the observed eddy-bloom
901 interaction is seen in the Southern part of the Arabian Sea.

902

903

904

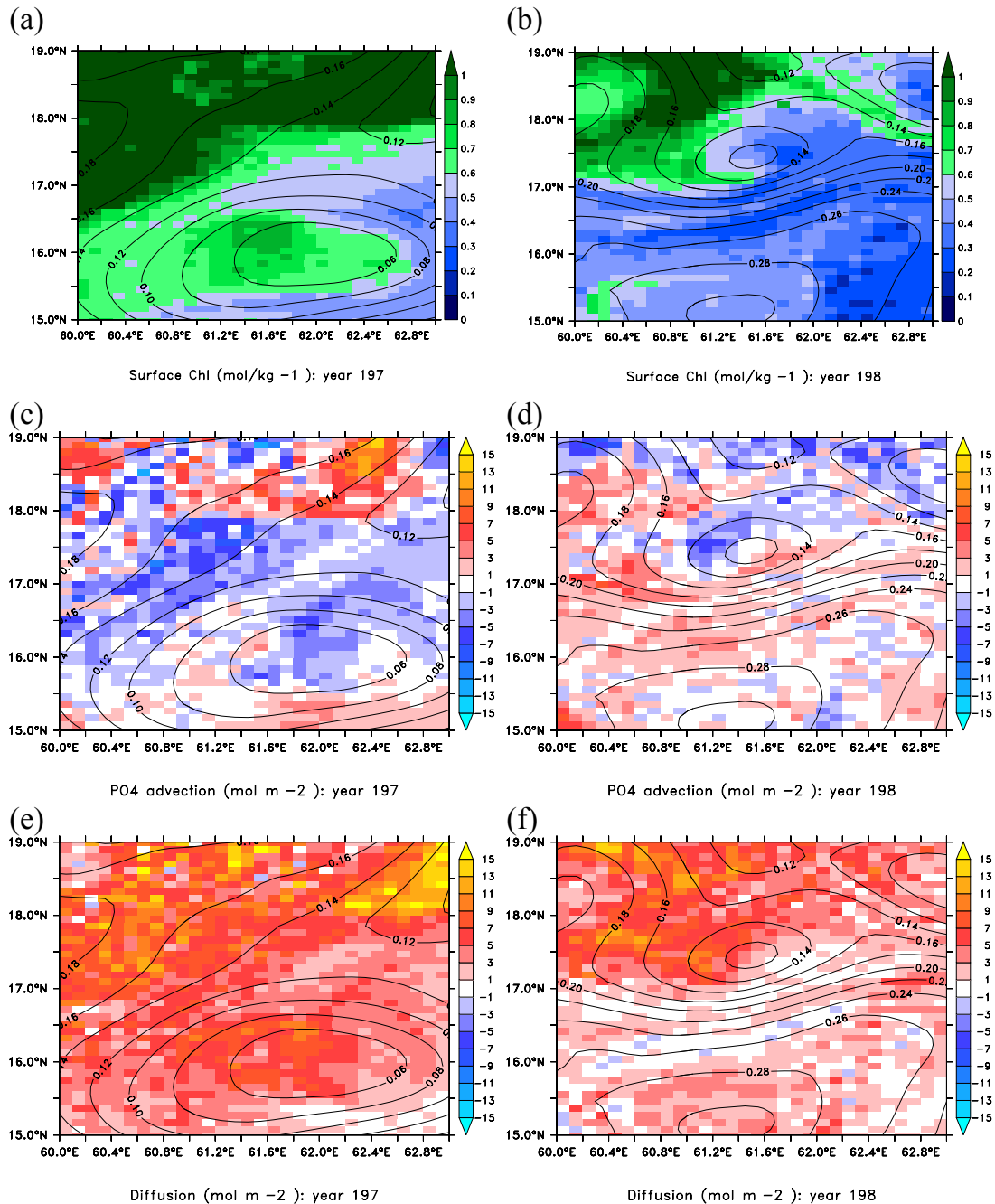


905

906
907
908

909 Figure 13. (a-d) Seawater temperature (°C) and Phosphate (PO₄) concentration (contours, μM)
910 for the northern (top row) and southern (middle row) parts of the central Arabian Sea. ; (e-f)
911 yearly averaged subsurface distribution of salinity (black contours) and potential density (red
912 contours). Left-hand column shows observations, right-hand column results from CM2.6
913 model.

914

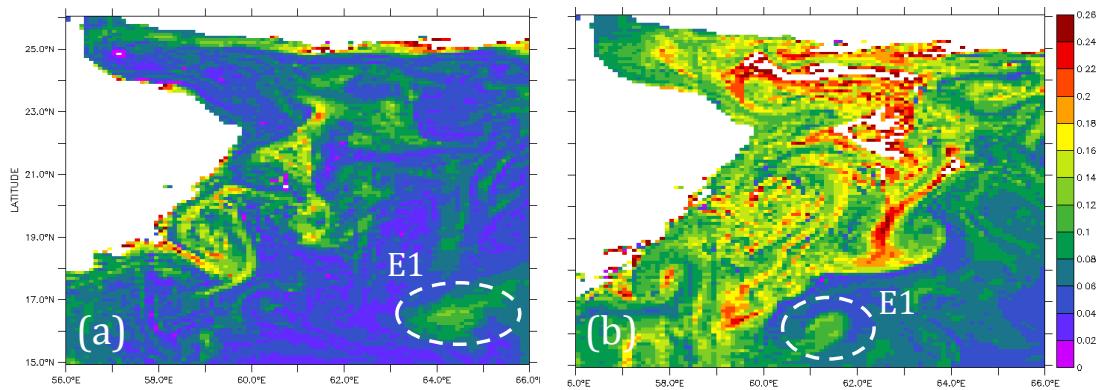


915

916 Figure 14. Surface chlorophyll in mg/m^3 . (a-b), Advection of phosphate to top 50m in
 917 mol/m^2 (c-d, colors), and diffusive flux of phosphate in mol/m^2 (e-f, colors) with sea surface
 918 height (contours, overlaid) for eddy E1 (63° - 66°E , 15° - 18°N) for the month of December
 919 during the two CM2.6 model years 197 and 198.

920

921



922

923 Figure 15. (a), (b) : CM2.6 (miniBLING) Po4 on 9 November and 28 December of year
924 197. (56° – 66° E, 15° – 26° N).

925